Thermo-Hydraulic Modelling and Experimental Validation of an Electro-Hydraulic Compact Drive

Ketelsen, Søren; Michel, Sebastian ; Andersen, Torben Ole; Ebbesen, Morten Kjeld; Weber, Jürgen ; Schmidt, Lasse

Published in:
Energies

DOI (link to publication from Publisher):
10.3390/en14092375

Publication date:
2021

Document Version
Publisher's PDF, also known as Version of record

energies

MDPI

Article

Thermo-Hydraulic Modelling and Experimental Validation of an Electro-Hydraulic Compact Drive

Søren Ketelsen [1,*], Sebastian Michel [2], Torben O. Andersen [1], Morten Kjeld Ebbesen [3], Jürgen Weber [2] and Lasse Schmidt [1]

[1] Department of Energy Technology, Aalborg University, 9220 Aalborg, Denmark; toa@et.aau.dk (T.O.A.); lsc@et.aau.dk (L.S.)
[2] Institute of Fluid Power (IFD), Technische Universität Dresden, 01069 Dresden, Germany; sebastian.michel@tu-dresden.de (S.M.); fluidtronik@mailbox.tu-dresden.de (J.W.)
[3] Department of Engineering Sciences, University of Agder, 4879 Grimstad, Norway; morten.k.ebbesen@uia.no
* Correspondence: sok@et.aau.dk; Tel.: +45-28-25-32-58

Abstract: Electro-hydraulic compact drives (ECDs) are an emerging technology for linear actuation in a wide range of applications. Especially within the low power range of 5–10 kW, the plug-and-play capability, good energy efficiency and small space requirements of ECDs render this technology a promising alternative to replace conventional valve-controlled linear drive solutions. In this power range, ECDs generally rely on passive cooling to keep oil and system temperatures within the tolerated range. When expanding the application range to larger power classes, passive cooling may not be sufficient. Research investigating the thermal behaviour of ECDs is limited but indeed required for a successful expansion of the application range. In order to obtain valuable insights into the thermal behaviour of ECDs, thermo-hydraulic simulation is an important tool. This may enable system design engineers to simulate thermal behaviour and thus develop proper thermal designs during the early design phase, especially if such models contain few parameters that can be determined with limited information available. Our paper presents a lumped thermo-hydraulic model derived from the conservation of mass and energy. The derived model was experimentally validated based on experimental data from an ECD prototype. Results show good accuracy between measured and simulated temperatures. Even a simple thermal model containing only a few thermal resistances may be sufficient to predict steady-state and transient temperatures with reasonable accuracy. The presented model may be used for further investigations into the thermal behaviour of ECDs and thus toward proper thermal designs required to expand the application range.

Keywords: thermal modelling; energy efficient fluid power; direct driven hydraulic drives; pump-controlled cylinder; electro-hydraulic compact drives; self-contained cylinder drive

Citation: Ketelsen, S.; Michel, S.; Andersen, T.O.; Ebbesen, M.K.; Weber, J.; Schmidt, L. Thermo-Hydraulic Modelling and Experimental Validation of an Electro-Hydraulic Compact Drive. *Energies* **2021**, *14*, 2375. https://dx.doi.org/10.3390/en14092375

Academic Editor: Davide Barater

Received: 21 March 2021
Accepted: 14 April 2021
Published: 22 April 2021

1. Introduction

Electro-hydraulic compact drives (ECDs) represent a promising alternative to conventional valve-controlled hydraulics as well as to electro-mechanical linear drive solutions [1–3]. By combining the robustness (including overload protection), high force density and high achievable transmission ratios of conventional hydraulic drives with the plug-and-play capabilities, better energy-efficiency and small space requirements of electro-mechanical linear drives, ECDs may be a competitive alternative in applications previously dominated by conventional technologies. As illustrated in Figure 1, ECDs basically consist of a variable-speed electric motor driving a fixed-displacement hydraulic pump. The pump outlets are connected to a differential cylinder, without any throttling elements, thus avoiding the associated immense power losses and enabling ECDs to recover energy in aided load situations. To balance the asymmetric cylinder flows, a low-pressure accumulator is often utilised to ensure appropriate suction conditions for the hydraulic pump. As opposed to valve-controlled drive solutions, the energy losses of ECDs are governed

by the energy efficiency of the components, as no inherent losses (i.e., valve throttling) are associated with the actuation principle.

During recent decades, the main research focus has been placed on identifying and investigating architectures that are able to connect the accumulator with the remaining circuit to facilitate operating in four quadrants. Two main topologies can be identified in research literature [4,5]. In valve-compensated architectures (Figure 1a), either hydraulically or electrically actuated valves are used to connect the low pressure cylinder chamber with the accumulator [6–8]. For pump-compensated architectures (Figure 1b), two or more pumps are matched to the areas of the differential cylinder to balance asymmetric flow without the need of valves [9–13]. To enable the ideal matching of pump displacements to the cylinder areas, independent of operating conditions, circuit architectures using two variable-speed electric motors (Figure 1c) are also being investigated [14,15]. A recent review highlighting the advantages and disadvantages of the considered architectures may be found in [16].

Some common drawbacks of the ECD technology potentially limiting its application range are currently being addressed by the research community. These include reliability and energy efficiency limitations in the low speed range of conventional hydraulic units [17–20], the challenge of incorporating load holding devices not affecting the ability of recovering energy in aided load situations [21–25] and identifying alternatives to the rather bulky gas-loaded accumulator [26,27]. The former challenge is also addressed by designing new types of hydraulic units, such that these are capable of low-speed operation at good efficiencies. The newly introduced AX series pump from Bucher Hydraulics is an example of such [28].

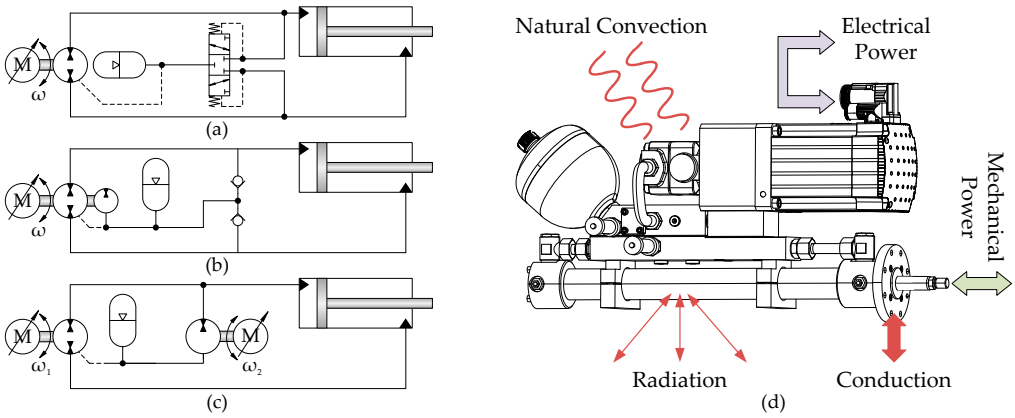

Figure 1. (**a**) Valve-compensated ECD. (**b**) Pump-compensated ECD. (**c**) ECD with two electric motors. (**d**) ECDs may rely solely on passive cooling.

The reported energy-efficiency of ECDs ranges from 50% up to 80% [29–31], but depends heavily on the working conditions. Nevertheless this is much higher than the energy efficiency of valve-controlled hydraulics, which features an average efficiency of 21% according to [32]. As opposed to conventional valve-controlled hydraulics where cooling devices are needed, the improved energy efficiency of ECDs may permit these systems to rely solely on passive cooling. This is illustrated in Figure 1d. The power losses of the system equals the passive heat transfer to the surroundings at an allowable equilibrium temperature. Passive cooling may be sufficient in the smaller power range of 5–10 kW, but for a higher power range it is unlikely that passive cooling suffices. Applications requiring larger power outputs, may among many other applications, include the actuation of large crane manipulators, where ECD architectures up to 80 kW or even bigger have been investigated by simulation studies in [33–35]. These studies however did not include thermal considerations. In the design phase of an ECD, it would be beneficial to understand the thermal behaviour of the system and to estimate to what extent cooling efforts are needed, prior to system realization. Nevertheless, research aiming at understanding and analysing the thermal behaviour of ECDs is limited. The authors in [36] measure

and compare efficiencies of a pump-compensated ECD, showing drastically reduced efficiencies at ambient temperatures below 0 °C. In [37,38], a thermo-hydraulic model is formulated in the commercially available software Simulation X, but compares this with measurements for a limited period of time, making it difficult to determine the accuracy of the model. In [39] a simple first order thermal model is proposed and used to actively control the average temperature of the system. It is unclear if the accuracy of the proposed thermal model is sufficient for system design purposes as well. In [40,41], a Simulation X model is formulated, and a good accuracy between measurements and simulation results is demonstrated. The parametrisation of the thermal model is elaborate, however, as a high number of solid thermal capacities are included. The current paper can be viewed as the continuation of the work in [40,41], as this paper investigates the trade-off between model complexity and accuracy based on the ECD system and experimental results presented in these references. The paper investigates two different thermal model complexities—the *benchmark* and the *reduced* model. The *benchmark* model is based on a relatively fine meshed discretization of the solid thermal capacities leading to an elaborate thermal submodel. On the other hand the *reduced* model features a more coarse discretization, leading to a simpler thermal model structure, making this suitable for design purposes.

The paper contributes to the research field by deriving the necessary equations, including descriptions of the fluid properties, needed to model the pressure and temperature dynamics of an ECD. Both of the considered model complexities were simulated using the equations derived in this paper to ensure comparability and full transparency. Note that the simulation results obtained in [40,41] are therefore not reused in this paper. To validate the derived models, these are compared to the experimental data obtained in [40,41].

For the mentioned references, the models are commonly based on a lumped parameter approach, which is also the case for this paper. This means that appropriate control volumes are defined assuming pressure and temperature to be homogeneous within the control volume [42]. This approach reduces the model complexity and needed computational effort greatly compared to finite element or computational fluid dynamics (CFD) methods, which are assessed to be too elaborate for system design purposes. Note that a system designer is desiring to roughly anticipate the system temperatures, and to do this with minimal effort and prior information.

The paper is organised as follows: In Section 2 the temperature and pressure dynamics of a lumped control volume are derived from first principles physics and in Section 3 consistent fluid properties of the oil–air mixture are derived. Section 4 presents the ECD prototype used for verification of the derived thermo-hydraulic model and Section 5 formulates the two thermal model complexities of the ECD prototype denoted the *benchmark* and *reduced* model. In Section 6, examples of calculating heat transfer resistances for basic geometries are given and used to parametrise the *reduced* model. Section 7 concludes the modelling part of the paper by deriving mass and enthalpy flow component models. Section 8 finally compares the simulation results of the two model complexities with experimental data. In the Nomenclature (Appendix A), the symbols used in the paper are listed.

2. Control Volume Dynamics

In this section, the pressure and temperature dynamics for a lumped control volume are derived from first principles physics, i.e., conservation of mass and energy. For a general control volume (CV), as seen in Figure 2, the continuity equation and the first law of thermodynamics may be written as Equations (1) and (2), respectively [43]:

$$\frac{\partial}{\partial t}\int_{\mathrm{cv}} \rho d\mathcal{V} + \int_{\mathrm{cs}} \rho \hat{\mathbf{V}} \cdot \hat{\mathbf{n}} dA = 0 \tag{1}$$

$$\frac{\partial}{\partial t}\int_{\mathrm{cv}} \left(u + \frac{\hat{V}^2}{2} + gz\right)\rho d\mathcal{V} + \int_{\mathrm{cs}} \left(u + \frac{\hat{V}^2}{2} + gz\right)\rho \hat{\mathbf{V}} \cdot \hat{\mathbf{n}} dA = \dot{Q} + \dot{W} \tag{2}$$

ρ is the fluid density, $\hat{\mathbf{V}}$ is the velocity vector of the fluid leaving the control volume across the control surface (CS) with normal vector $\hat{\mathbf{n}}$. Thus, the mass flow leaving the control volume is positive. u is specific internal energy, $\hat{V}^2/2$ and gz are kinetic energy and potential energy per unit mass, respectively. $\dot{Q}$ and $\dot{W}$ are heat flow transferred to and net rate of work done on the system, respectively.

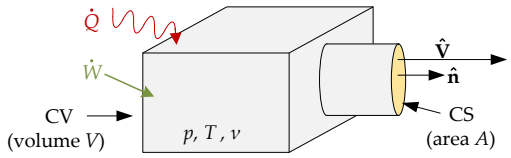

Figure 2. Illustration of a lumped control volume. Pressure, temperature and specific volume are assumed to be homogeneous. Mass transfer may occur across the control surface (CS).

2.1. Lumped Pressure Dynamics

Consider Equation (1), and assume that the density is homogeneous in the CV and on the CS. Allowing for mass exchange to occur across multiple control surfaces leads to the following simplification of the continuity equation in Equation (1):

$$\frac{\partial}{\partial t}(\rho V) + \sum_k \dot{m}_k - \sum_i \dot{m}_i = 0 \quad \Leftrightarrow \quad \dot{m} = \sum_i \dot{m}_i - \sum_k \dot{m}_k \quad \Leftrightarrow \quad \dot{\rho} V + \rho \dot{V} = \dot{m} \tag{3}$$

where V is the volume of the CV, and the index i is used to sum over incoming mass flows while k denotes leaving mass flows, such that $\dot{m} = \sum_i \dot{m}_i - \sum_k \dot{m}_k$. The density is an intensive property and may, by the state postulate, be expressed as a function of two independent intensive properties e.g., temperature and pressure. A change in density may be established by the total differential [44]:

$$\rho = f(p,T) \quad \Rightarrow \quad d\rho = \left(\frac{\partial \rho}{\partial p}\right)_{\mathrm{T}} dp + \left(\frac{\partial \rho}{\partial T}\right)_{\mathrm{p}} dT \quad \Rightarrow \quad \dot{\rho} = \left(\frac{\partial \rho}{\partial p}\right)_{\mathrm{T}} \dot{p} + \left(\frac{\partial \rho}{\partial T}\right)_{\mathrm{p}} \dot{T} \tag{4}$$

The partial derivatives in Equation (4) may be expressed using material properties, recognizing that the isothermal bulk modulus β and the isobaric expansion coefficient α are defined as [45,46]:

$$\beta = -V\left(\frac{\partial p}{\partial V}\right)_{\mathrm{T}} = \rho\left(\frac{\partial p}{\partial \rho}\right)_{\mathrm{T}} = \frac{\rho}{\left(\frac{\partial \rho}{\partial p}\right)_{\mathrm{T}}} \qquad \alpha = \frac{1}{\nu}\left(\frac{\partial \nu}{\partial T}\right)_{\mathrm{p}} = -\frac{1}{\rho}\left(\frac{\partial \rho}{\partial T}\right)_{\mathrm{p}} \tag{5}$$

where ν is the specific volume ($\nu = \rho^{-1}$). Substituting Equation (4) into Equation (3) combined with the material properties from Equation (5), and isolating for $\dot{p}$ yield:

$$\left(\frac{\rho}{\beta}\dot{p} - \alpha\rho\dot{T}\right)V + \rho\dot{V} = \dot{m} \qquad \Leftrightarrow \qquad \dot{p} = \frac{\beta}{V}\left(\frac{\dot{m}}{\rho} - \dot{V} + \alpha V \dot{T}\right) \tag{6}$$

Hence, the pressure dynamics of a lumped control volume is given by Equation (6).

2.1.1. Mechanical Elasticity

To include mechanical elasticity, i.e., expanding hoses or pipes for increasing pressures, the volume in Equation (6) is calculated as:

$$V = V_{\mathrm{x}}\left(1 + \frac{p - p_0}{\beta_{\mathrm{mech}}}\right) \qquad \Rightarrow \qquad \dot{V} = \dot{V}_{\mathrm{x}}\left(\frac{p - p_0}{\beta_{\mathrm{mech}}}\right) + \frac{V_{\mathrm{x}}}{\beta_{\mathrm{mech}}}\dot{p} \tag{7}$$

where V_{x} is the volume at p_0, and may include a fixed volume as well as a time dependent volume, e.g., a stoke dependent volume if the control volume is a cylinder chamber. β_{mech} is

a tuning parameter such that a high value of β_{mech} corresponds to a stiff volume, whereas a low value corresponds to an elastic volume. Inserting Equation (7) into Equation (6) yields:

$$\dot{p} = \underbrace{\left(\frac{\beta \beta_{mech}}{\beta_{mech} + \beta \frac{\beta_{mech}}{\beta_{mech} + p - p_0}} \right)}_{\beta_{eff}} \left(\frac{\dot{m}}{\rho V} - \frac{\dot{V}_x}{V_x} + \alpha \dot{T} \right) \tag{8}$$

where β_{eff} is the effective bulk modulus, including the effect of mechanical elasticity. If β_{mech} approaches infinity, β_{eff} approaches β and V_x approaches V, such that Equation (8) approaches Equation (6).

2.1.2. Diaphragm and Bladder Accumulators

Control volumes contained in a gas-loaded diaphragm or bladder accumulator are modelled without including mechanical elasticity. This is appropriate because nitrogen is much more compliant than the mechanical structures. For ECDs, the accumulator is operated at low pressures and room temperatures, i.e., far away from the critical point [46], justifying nitrogen to be modelled as an ideal gas. The volume and $\dot{V}$ of the oil in the accumulator control volume are therefore found as:

$$V = V_{acc} + V_x - V_{gas} \qquad \dot{V} = \dot{V}_x - \dot{V}_{gas} \tag{9}$$

$$V_{gas} = \frac{V_{acc} p_{acc0} T_{gas}}{T_{acc0} p} \qquad \dot{V}_{gas} = \frac{V_{gas}}{T_{gas}} \dot{T}_{gas} - \frac{V_{gas}}{p} \dot{p} \tag{10}$$

where V_{acc} is the accumulator volume (constant), V_{gas} is the gas volume, and V_x is the oil volume outside the accumulator shell, which may include a fixed volume or a volume changing in time. T_{gas} is the gas temperature and finally p_{acc0} and T_{acc0}, are the precharge pressure and temperature, respectively. Assuming the gas and oil pressure to be equal, and by combining Equation (10) with Equation (6) yield $\dot{p}$ as:

$$\dot{p} = \frac{p\beta}{pV + \beta V_{gas}} \left(\frac{\dot{m}}{\rho} - \dot{V}_x + \alpha V \dot{T} + \frac{V_{gas}}{T_{gas}} \dot{T}_{gas} \right) \tag{11}$$

Note that T is the oil temperature and T_{gas} is the gas temperature. It can be seen that if the accumulator is removed (V_{acc} = 0) Equation (11) equals Equation (6).

The gas temperature may be assumed to equal the temperature of the accumulator shell, by assuming the gas compression to be an isothermal process. However, to include temperature changes due to compression, consider the first law of thermodynamics in Equation (2). Assume the density to be homogeneous within the control volume, the kinetic and potential energies to be negligible and acknowledge that mass is not exchanged across the control surfaces:

$$\dot{u} m_{gas} = \dot{U} = \dot{Q} + \dot{W} \quad , \quad U(p, V) \Rightarrow \tag{12}$$

$$dU = \left(\frac{\partial U}{\partial T_{gas}} \right)_V dT_{gas} + \left(\frac{\partial U}{\partial V_{gas}} \right)_T dV_{gas} = m_{gas} c_v dT_{gas} + \left(T_{gas} \left(\frac{\partial p}{\partial T_{gas}} \right)_V - p \right) dV_{gas} \Rightarrow$$

$$\dot{U} = m_{gas} c_v \dot{T}_{gas} + \left(\beta \alpha T_{gas} - p \right) \dot{V}_{gas} \xrightarrow{\text{Ideal Gas}} \dot{U} = m_{gas} c_v \dot{T}_{gas} \tag{13}$$

where U is internal energy of the gas, m_{gas} is the mass of the gas and c_v is the isochoric specific heat. Equation (13) originates from the state postulate by taking the total differential of the internal energy as a function of pressure and volume and expressing the partial derivatives using fluid properties [47]. For ideal gasses $\beta = p$ and $\alpha = T^{-1}$ leading to

$\dot{U} = m_{\text{gas}} c_{\text{v}} \dot{T}$. Recognizing the rate of work done on the gas is by compression ($\dot{W} = -p\dot{V}_{\text{gas}}$) and combining Equations (12) and (13) yield the gas temperature dynamics as:

$$\left.\begin{aligned} \dot{T}_{\text{gas}} &= \tfrac{1}{m_{\text{gas}} c_{\text{v}}} \left(\dot{Q} - p\dot{V}_{\text{gas}} \right) \\ \dot{Q} &= hA\left(T_{\text{acc}} - T_{\text{gas}} \right) = \tfrac{m_{\text{gas}} c_{\text{v}}}{\tau} \left(T_{\text{acc}} - T_{\text{gas}} \right) \end{aligned} \right\} \Rightarrow \dot{T}_{\text{gas}} = \frac{\left(T_{\text{acc}} - T_{\text{gas}} \right)}{\tau} - \frac{p}{m_{\text{gas}} c_{\text{v}}} \dot{V}_{\text{gas}} \tag{14}$$

Instead of calculating the transferred heat $\dot{Q}$ using the convection heat transfer coefficient h and the surface area A, $\dot{Q}$ is modelled using a fixed thermal time constant defined as $\tau = \frac{m_{\text{gas}} c_{\text{v}}}{hA}$ [48–50]. T_{acc} is the temperature of the accumulator shell.

2.2. Lumped Temperature Dynamics

For hydrostatic transmission systems kinetic and potential energies are small compared to internal energy and flow work (enthalpy) and thus neglected [41,51] in the first law of thermodynamics in Equation (2). Additionally, the assumptions given in Section 2.1 are imposed, i.e., assuming uniform density and specific internal energy distribution in the control volume and on the control surfaces. By allowing mass transfer to occur from several control surfaces Equation (2) simplifies to:

$$\frac{\partial}{\partial t}(\rho V u) - \sum_i \dot{m}_i u_i + \sum_k \dot{m}_k u = \dot{Q} + \dot{W} \tag{15}$$

$$\dot{m}u + m\dot{u} - \sum_i \dot{m}_i u_i + \sum_k \dot{m}_k u = \dot{Q} + \dot{W} \tag{16}$$

$$\sum_i \dot{m}_i u - \sum_k \dot{m}_k u + m\dot{u} - \sum_i \dot{m}_i u_i + \sum_k \dot{m}_k u = \dot{Q} + \dot{W} \tag{17}$$

$$\sum_i \dot{m}_i (u - u_i) + m\dot{u} = \dot{Q} + \dot{W} \tag{18}$$

Defining specific enthalpy as $h = u + pv$, the term $m\dot{u}$ can be rewritten to $m\dot{u} = m(\dot{h} - \dot{p}v - \dot{v}p)$. $\dot{h}$ is expressed as a function of temperature and pressure [52]:

$$dh = \left(\frac{\partial h}{\partial T} \right)_{\text{p}} dT + \left(\frac{\partial h}{\partial p} \right)_{\text{T}} dp = c_{\text{p}} dT + \left(v - T\left(\frac{\partial v}{\partial T} \right)_{\text{p}} \right) dp \tag{19}$$

$$= c_{\text{p}} dT + v(1 - T\alpha) dp \qquad \Rightarrow \qquad \dot{h} = c_{\text{p}} \dot{T} + (1 - T\alpha) v\dot{p} \tag{20}$$

The partial derivatives are rewritten using material properties based on [47,52,53]. Inserting Equation (20) into $m\dot{u} = m(\dot{h} - \dot{p}v - \dot{v}p)$ leads to:

$$m\dot{u} = m(\dot{h} - \dot{p}v - \dot{v}p) = m(c_{\text{p}} \dot{T} + (1 - T\alpha) v\dot{p} - \dot{p}v - \dot{v}p) = mc_{\text{p}} \dot{T} - m\dot{v}p - T\alpha V\dot{p} \tag{21}$$

$\dot{W}$ in Equation (18) has the form of either rate of shaft work, rate of moving boundary work (MBW) or rate of flow work [54]:

$$\dot{W} = \dot{W}_{\text{shaft}} - \underbrace{p\dot{V}}_{\text{MBW}} + \underbrace{\sum_i p_i A_i \hat{V}_i - \sum_k p A_k \hat{V}_k}_{\text{flow work}} = \dot{W}_{\text{shaft}} - \underbrace{m\dot{v}p - \dot{m}vp}_{\text{MBW}} + \underbrace{\sum_i \dot{m}_i p_i v_i - \sum_k \dot{m}_k pv}_{\text{flow work}}$$

$$= \dot{W}_{\text{shaft}} - m\dot{v}p - \left(\sum_i \dot{m}_i - \sum_k \dot{m}_k \right) vp + \sum_i \dot{m}_i p_i v_i - \sum_k \dot{m}_k pv \tag{22}$$

$$= \dot{W}_{\text{shaft}} - m\dot{v}p + \sum_i \dot{m}_i (p_i v_i - pv) \tag{23}$$

Inserting Equations (21) and (23) in Equation (18), and isolating for the temperature derivative:

$$\sum_i \dot{m}_i(u-u_i) + mc_p\dot{T} - T\alpha V\dot{p} - m\dot{v}p = \dot{Q} + \dot{W}_{\text{shaft}} + \sum_i \dot{m}_i(p_i v_i - pv) - m\dot{v}p \tag{24}$$

$$\sum_i \dot{m}_i(h-h_i) + mc_p\dot{T} - T\alpha V\dot{p} = \dot{Q} + \dot{W}_{\text{shaft}} \tag{25}$$

$$\dot{T} = \frac{1}{mc_p}\left(\dot{Q} + \dot{W}_{\text{shaft}} + \sum_i \dot{m}_i(h_i - h) + T\alpha V\dot{p}\right) \tag{26}$$

Thus, the temperature dynamic of a lumped control volume is given by Equation (26).

3. Fluid Properties

The pressure and temperature dynamics in the previous section were derived from the conservation of mass and energy. For this to be upheld during a numerical simulation, the material properties need to fulfil the relationships stated in Equation (5). One approach for doing so is to use a density description as the starting point for deriving the remaining mass/volume related properties. The oil density, ρ_F is modelled as a function of pressure and temperature and approximated by a first order Taylor series expansion:

$$\rho_F = \rho_{F0}\left(1 + \frac{p-p_0}{\beta_0} - \rho_{F0}\alpha_0(T-T_0)\right) \tag{27}$$

where ρ_{F0}, β_0 and α_0 are oil properties at T_0 = 288.15 K and p_0 = 101,325 Pa. Especially at low pressures, free air present in the oil affects the fluid properties. To include this, the density of the free air ρ_A is modelled as an ideal gas, compressed during a polytropic process [46]:

$$\rho_A = \frac{p}{RT_1} \qquad T_1 = \left(\frac{p_0}{p}\right)^{\frac{1-\kappa}{\kappa}} T \tag{28}$$

where R is the gas constant for air , T_1 is the air temperature at the current pressure p, assuming polytropic compression from p_0 with polytropic coefficient κ. T is the lumped temperature of the oil–air mixture. The density of the oil–air mixture is found as:

$$\rho = \frac{m}{V} = \frac{V_{A0}\rho_{A0} + V_{F0}\rho_{F0}}{V_A + V_F} = \frac{V_{A0}\rho_{A0} + V_{F0}\rho_{F0}}{\frac{m_A}{\rho_A} + \frac{m_F}{\rho_F}} = \frac{V_{A0}\rho_{A0} + V_{F0}\rho_{F0}}{\frac{V_{A0}\rho_{A0}}{\rho_A} + \frac{V_{F0}\rho_{F0}}{\rho_F}} \tag{29}$$

where ρ_{A0}, V_{A0} and V_{F0} are the air density and the volumes occupied by air and oil at p_0 and T_0, respectively. ϵ is defined as the volumetric ratio of air in the mixture at p_0 and T_0, such that Equation (29) rewrites to:

$$\left.\begin{array}{l} V_{A0} = \epsilon V_0 \\ V_{F0} = (1-\epsilon)V_0 \end{array}\right\} \Rightarrow \rho = \frac{\epsilon V_0\rho_{A0} + (1-\epsilon)V_0\rho_{F0}}{\frac{\epsilon V_0\rho_{A0}}{\rho_A} + \frac{(1-\epsilon)V_0\rho_{F0}}{\rho_F}} = \frac{\epsilon\rho_{A0} + (1-\epsilon)\rho_{F0}}{\frac{\epsilon\rho_{A0}}{\rho_A} + \frac{(1-\epsilon)\rho_{F0}}{\rho_F}} \tag{30}$$

The mixture density can thus be written as a function of pressure and temperature:

$$\rho = \frac{C_1 f_1}{p_0^{\frac{1}{\kappa}} p^{-\frac{1}{\kappa}} T f_1 \epsilon + (\epsilon - 1)\beta_0 T_0} \qquad \begin{array}{c} C_1 = T_0(\rho_{F0} + (\rho_{A0} - \rho_{F0})\epsilon) \\ f_1 = (\alpha_0(T - T_0 - 1))\beta_0 - p + p_0 \end{array} \tag{31}$$

The bulk modulus β, and expansion coefficient α of the mixture are found from the definitions in Equation (5):

$$\beta = \frac{\rho}{\left(\frac{\partial \rho}{\partial p}\right)_T} = \frac{f_1 \kappa p \left(p_0^{\frac{1}{\kappa}} T \epsilon f_1 + p^{\frac{1}{\kappa}} \beta_0 T_0 (\epsilon - 1) \right)}{T p_0^{\frac{1}{\kappa}} \epsilon f_1^2 - T_0 \kappa \beta_0 (\epsilon - 1) p^{\frac{1+\kappa}{\kappa}}} \tag{32}$$

$$\alpha = \frac{f_1 p_0^{\frac{1}{\kappa}} \left(\epsilon^2 T p_0^{\frac{1}{\kappa}} f_1^2 - T_0 \beta_0 p^{\frac{1}{\kappa}} \left(\epsilon^2 - \epsilon \right) (T \alpha_0 \beta_0 - f_1) \right) - \alpha_0 T_0^2 \beta_0^3 (\epsilon - 1)^2 p^{\frac{2}{\kappa}}}{\left(\epsilon T p_0^{\frac{1}{\kappa}} f_1 + p^{\frac{1}{\kappa}} \beta_0 T_0 (\epsilon - 1) \right)^2 f_1} \tag{33}$$

The specific heat, c_p, is considered only for the oil due to a small mass fraction of air in the mixture. A volume fraction of air of 10% ($\epsilon = 0.1$) at atmospheric pressure yields a mass fraction of air less than 0.2%. The specific heat is assumed to be only a function of temperature, and is given for a HLP32 oil in [55] as:

$$c_p = c_{p0} + K_{cp} T \tag{34}$$

c_{p0} and K_{cp} are modelling parameters found in Appendix B. The specific enthalpy of the oil–air mixture is approximated by the differential equation in Equation (19) as a finite difference [56]:

$$\Delta h \cong \bar{c}_p \Delta T + \frac{1 - \bar{\alpha} \bar{T}}{\bar{\rho}} \Delta p \qquad \Rightarrow \qquad h \cong \bar{c}_p (T - T_0) + \frac{1 - \bar{\alpha} \left(\frac{T_0 + T_1}{2} \right)}{\bar{\rho}} (p - p_0) \tag{35}$$

where the notation $\bar{\bullet}$ denotes material properties evaluated at the mean temperature and pressure. The specific enthalpy equals 0 J/kg at T_0=288.15 K , and p_0=101325 Pa.

In order to calculate the thermal resistances in Section 6, additional fluid properties are needed, including the dynamic viscosity, μ, and thermal conductivity, k. These are modelled as oil properties, i.e., without considering the air in the mixture. The dynamic viscosity of an HM46 oil is modelled by the Vogel–Barus model [57], and the thermal conductivity is calculated as a first order polynomial using fluid properties extracted as a function of temperature from the Equation Engineering Solver (EES, V10.836) library:

$$\mu = a_{\mu 1} \mathrm{e}^{\left(\frac{a_{\mu 2}}{T - a_{\mu 3}} \right)} \mathrm{e}^{\left(\frac{p}{a_{\mu 4} + a_{\mu 5} (T - 273.15)} \right)} \qquad k = a_{k1} - a_{k2} T \tag{36}$$

where $a_\bullet$ are modelling coefficients that are given in Appendix B.

3.1. Temperature Independent Density

The temperature and pressure dynamics derived in Section 2 (Equations (6) and (26)), are coupled via the thermal expansion coefficient α. As the numerical value of α is small ($\approx$0.0007 K^{-1}), the coupling between the pressure and temperature dynamics may be neglected without sacrificing much accuracy in terms of the main dynamics [56]. To simplify the model formulation, it is profitable to decouple pressure and temperature dynamics by assuming α = 0. However for mass to be conserved, the remaining volume and mass related properties (ρ and β) must be consistent with this assumption. This can be obtained by assuming the density of oil and air only being pressure dependent, such that:

$$\tilde{\rho}_F = \tilde{\rho}_{F0} \left(1 + \frac{p - p_0}{\beta_0} \right) \qquad \tilde{\rho}_A = \frac{p}{R T_0} \tag{37}$$

where the notation $\tilde{\bullet}$ denotes properties assumed to be temperature independent. By Equation (37), the temperature independent properties can be expressed as:

$$\tilde{\rho} = \frac{(\tilde{\rho}_{F0} + (\tilde{\rho}_{A0} - \tilde{\rho}_{F0})\epsilon)(\beta_0 + p - p_0)p}{(p_0 - \beta_0)(p - p_0)\epsilon + \beta_0 p} \tag{38}$$

$$\tilde{\beta} = \frac{p((p_0 - \beta_0)(p - p_0)\epsilon + \beta_0 p)(\beta_0 + p + p_0)}{\left(p_0^2 - (\beta_0 + 2p)p_0 + p^2\right)(p_0 - \beta_0)\epsilon + \beta_0 p_0} \tag{39}$$

The definitions in Equations (38) and (39) yield $\tilde{\alpha} = 0$, as desired.

3.2. Comparing Modelled and Measured Fluid Properties

In [55], the density of an HLP 32 oil was measured as a function of temperature and pressure. These measurements are used to fit the parameters of ρ_{F0}, β_0 and α_0 in Equation (27). In Figure 3a, a good fit between the modelled density and the measurements from [55] is observed. In the plot, the density of the oil–air mixture is also shown. The bulk modulus and thermal expansion coefficients are shown in Figure 3b,c. Figure 3b includes the effective bulk modulus, β_{eff}, considering mechanical elasticity, as introduced in Equation (8). Introducing mechanical elasticity lowers the bulk modulus compared to just considering the oil–air mixture.

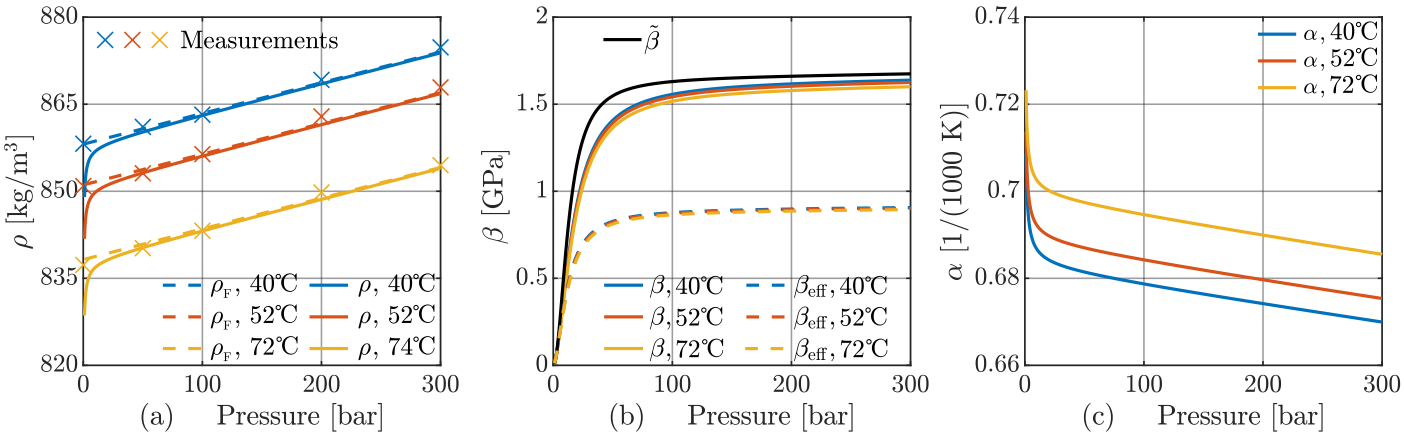

Figure 3. Fluid properties evaluated with a volumetric air content of 1%. (**a**) Dashed lines are modelled oil densities and solid lines are oil–air mixture densities. Measurements are obtained from [55]. (**b**) Modelled oil–air mixture bulk moduli. Dashed lines include the effect of mechanical elasticity with $\beta_{mech} = 2\,\text{GPa}$. $\tilde{\beta}$ is the temperature independent bulk modulus. (**c**) Modelled thermal expansion coefficient of oil–air mixture.

This concludes the derivation of the lumped thermo-hydraulic model, including definition of consistent fluid properties. Models of the heat, mass and enthalpy flows entering the control volumes are defined subsequently. The ECD prototype used for experimental investigation is introduced next.

4. Electro-Hydraulic Compact Drive Prototype

The ECD prototype shown in Figure 4 was manufactured and tested at the Technical University of Dresden, Germany. The cylinder of the prototype was flanged on a general purpose test-rig, with the rod being connected to a load cylinder capable of loading the ECD with varying load forces. The ECD was connected with the load cylinder via an inertia mass of 110 kg, which is not shown in Figure 4. On the cylinder, a manifold was mounted, which connects the cylinder chambers with the pump and a diaphragm accumulator using an inverse shuttle valve for flow balancing. The pump was driven by a brushless DC motor. The pump and motor shafts were connected through the adapter plate. The adapter plate and accumulator were mounted on the manifold, such that the ECD forms a self-contained and compact drive system. The hydraulic diagram showing the main components of the

prototype is given in Figure 5a. The prototype was a valve-compensated ECD, meaning that the inverse shuttle valve (ISV) connects the low pressure side of the cylinder with the low pressure accumulator, such that the asymmetric cylinder flow was balanced. Further information regarding the design and performance of the ECD prototype is available in [1,40,41,58].

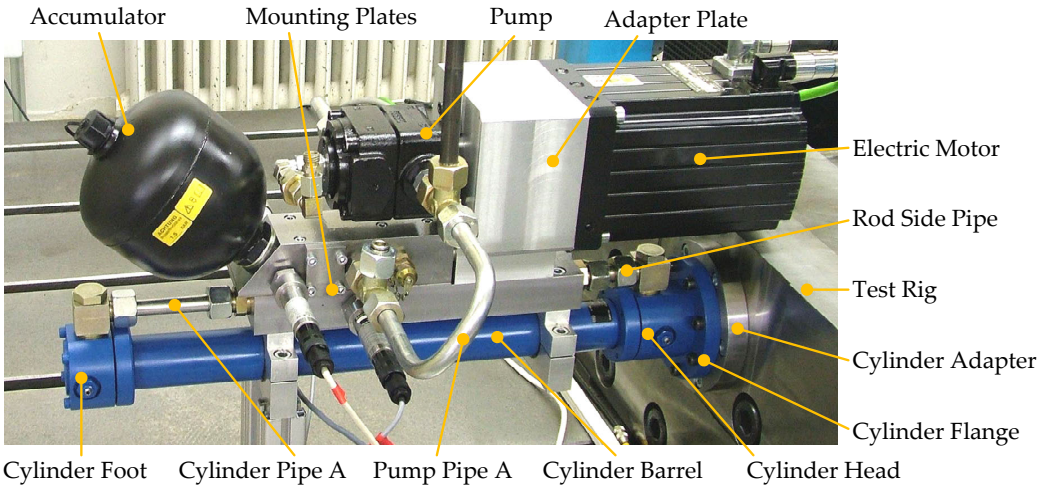

Main Components

Component	Description	Component	Description
Differential Cylinder	Rexroth CDM1 (40/22–450 mm)	Inverse shuttle valve	HydraForce HS50-43
Internal Gear Pump	Bucher QXM22-006 (6.3 cm^3/rev)	Servo Motor	Moog Series G
Accumulator	1.4 L Accumulator	Mounting Plates	Custom Made

Figure 4. ECD prototype manufactured at TU-Dresden. The table lists the main components of the system.

For the experiments conducted in this study, a positive load force was present at all times, which means that the ISV connected the accumulator with the cylinder rod chamber at all times. The switching dynamics of the ISV was therefore not included, and the ISV was approximated by an orifice as shown in Figure 5b. The mass flow names used when formulating the model in the upcoming section, and the positions of the oil temperature sensors mounted on the prototype are shown.

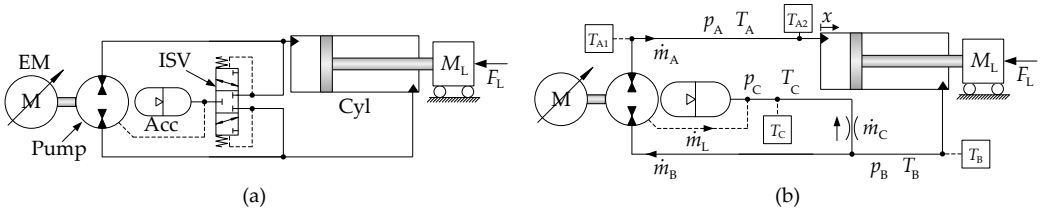

Figure 5. (**a**) Diagram showing the main components of the ECD prototype. (**b**) Simplified schematic, valid for the conducted experiments, and used during formulation of the thermo-hydraulic model. The simplified schematic also shows the position of the oil temperature sensors on the prototype.

5. Thermo-Hydraulic Model Formulation

In this section, the lumped thermo-hydraulic model derived in Section 2, is utilised to model the pressure and temperature dynamics of the ECD prototype, presented in the previous section.

Two model complexities are presented subsequently. The model denoted *benchmark* model, utilises a relatively fine meshed discretization of lumped solid thermal capacities, including all of the named components in Figure 4. To describe the heat transfers occurring internally in the system and to the surroundings an extensive thermal resistance network

is defined. This thermal network was developed in previous publications [40,41], and is used here as a benchmark for model validation and for comparison with a simpler model complexity, i.e., the *reduced* model.

In the *reduced* model, a significantly coarser discretization is utilised. In [40,41], the forced convection resistances were found to be negligible, as the thermal behaviour was governed by natural convection and radiation from the system to the surroundings. Therefore, the *reduced* model investigates, among other things, how model accuracy is affected by neglecting forced convection resistances. Neglecting the forced convection resistances may be done in several ways. If commercial simulation software is used, arbitrary small forced convection resistances may be defined to maintain the number of lumped temperatures. Alternatively, the temperature dynamics of multiple fluid and solid control volumes may be lumped together, thus reducing the number of temperature states in the model. The latter approach is featured here. As the temperature dynamics of multiple fluid volumes are lumped together, it is beneficial to neglect the coupling between the temperature and pressure dynamics by utilising temperature independent fluid properties, as given in Section 3.1.

Table 1 compares the two model complexities.

Table 1. Comparison of the two model complexities.

	Model Complexity	
	Benchmark	**Reduced**
Fluid Properties	Temperature Dependent (Equations (31)–(33))	Temperature Independent $\tilde{\alpha} = 0$ and Equations (38) and (39)
Number of Thermal Capacities	3 Oil Capacities 18 Solid Capacities	1 Combined Oil/Solid Capacity 1 Oil Capacity & 1 Solid Capacity
Number of Thermal Resistances	18 Natural Convection & Radiation 21 Conduction Resistances 23 Forced Convection Resistances	5 Natural Convection & Radiation 1 Conduction Resistance 1 Forced Convection Resistance

The reason for dealing with two model complexities is to investigate how much information and accuracy are lost when reducing the model complexity. As seen from Table 1, the current study especially investigates the needed level of detail for the thermal submodels, including the number of thermal resistances used to model heat transfers in the system. The *benchmark* model demonstrated a good ability to provide accurate temperature simulations for most of the thermal capacities in [41]. However, parametrising the 62 thermal resistances present in the *benchmark* model is both a time-consuming and tedious task. In addition, for instance, the forced convection resistances occurring in the flow channels of a custom made manifold requires detailed knowledge about the construction of this to parametrise the resistances. Such detailed information may not be available during the design phase, where a design engineer desires to estimate the operating temperature for a given ECD under some loading conditions. To address the potential challenges of the *benchmark* model, a drastically reduced model, which requires limited information for parametrisation, was investigated. This includes cylinder and accumulator dimensions as well as approximate dimensions of manifold, pump and electric motor. As such, the current investigation may be regarded as a natural next step toward a simple but yet sufficiently accurate model level. The authors claim that if a thermo-hydraulic model should be useful for a design engineer, it should be relatively easy to parametrise even though this may decrease the accuracy. By the end of the day, approximate estimations or rough ideas are more useful than very accurate simulations that are never carried out due to time-consuming model development or parameters unknown during the design phase. Estimating the operating temperature is important to determine to what extent cooling is required, i.e., to obtain a proper thermal design. This may include the addition of a fan, heat pipes mounted in the manifold, an oil cooler or a water cooled manifold.

The following sections show the derivation of the two model complexities, with an offset in the system diagram in Figure 5b.

5.1. Benchmark Model

The pressure dynamics of the *benchmark* model are formulated as:

$$\dot{p}_{\mathrm{A}} = \frac{\beta_{\mathrm{A}}\beta_{\mathrm{mech}}}{\beta_{\mathrm{mech}} + \beta_{\mathrm{A}}\frac{\beta_{\mathrm{mech}}}{\beta_{\mathrm{mech}}+p_{\mathrm{A}}-p_0}}\left(\frac{\dot{m}_{\mathrm{A}}}{\rho_{\mathrm{A}}V_{\mathrm{A}}} - \frac{\dot{x}A_{\mathrm{A}}}{V_{\mathrm{Ax}}} + \alpha_{\mathrm{A}}\dot{T}_{\mathrm{A}}\right), \quad \begin{aligned} V_{\mathrm{Ax}} &= V_{\mathrm{A0}} + xA_{\mathrm{A}} \\ V_{\mathrm{A}} &= V_{\mathrm{Ax}}\left(1+\frac{p_{\mathrm{A}}-p_0}{\beta_{\mathrm{mech}}}\right)\end{aligned} \tag{40}$$

$$\dot{p}_{\mathrm{B}} = \frac{\beta_{\mathrm{B}}\beta_{\mathrm{mech}}}{\beta_{\mathrm{mech}} + \beta_{\mathrm{B}}\frac{\beta_{\mathrm{mech}}}{\beta_{\mathrm{mech}}+p_{\mathrm{B}}-p_0}}\left(\frac{-\dot{m}_{\mathrm{B}}-\dot{m}_{\mathrm{C}}}{\rho_{\mathrm{B}}V_{\mathrm{B}}} + \frac{\dot{x}A_{\mathrm{B}}}{V_{\mathrm{Bx}}} + \alpha_{\mathrm{B}}\dot{T}_{\mathrm{B}}\right), \quad \begin{aligned} V_{\mathrm{Bx}} &= V_{\mathrm{B0}} + (L_{\mathrm{s}}-x)A_{\mathrm{B}} \\ V_{\mathrm{B}} &= V_{\mathrm{Bx}}\left(1+\frac{p_{\mathrm{B}}-p_0}{\beta_{\mathrm{mech}}}\right)\end{aligned} \tag{41}$$

$$\dot{p}_{\mathrm{C}} = \frac{p_{\mathrm{C}}\beta_{\mathrm{C}}}{p_{\mathrm{C}}V_{\mathrm{C}} + \beta_{\mathrm{C}}V_{\mathrm{gas}}}\left(\frac{\dot{m}_{\mathrm{L}}+\dot{m}_{\mathrm{C}}}{\rho_{\mathrm{C}}} + \alpha_{\mathrm{C}}V_{\mathrm{C}}\dot{T}_{\mathrm{C}} + \frac{V_{\mathrm{gas}}}{T_{\mathrm{gas}}}\dot{T}_{\mathrm{gas}}\right), \quad \begin{aligned} V_{\mathrm{C}} &= V_{\mathrm{Acc}} + V_{\mathrm{C0}} - V_{\mathrm{gas}} \\ V_{\mathrm{gas}} &= \frac{V_{\mathrm{Acc}}p_{\mathrm{acc0}}T_{\mathrm{gas}}}{T_{\mathrm{acc0}}p_{\mathrm{C}}}\end{aligned} \tag{42}$$

The subscripts {A, B, C} in Equations (40)–(42) refer to the piston chamber, the rod side chamber and the accumulator, respectively, according to Figure 5b.

The gas temperature is modelled using Equation (14). The temperature dynamics of the oil control volumes are modelled from Equation (26) as:

$$\dot{T}_{\mathrm{A}} = \frac{1}{V_{\mathrm{A}}\rho_{\mathrm{A}}c_{\mathrm{p,A}}}\left(\dot{Q}_{\mathrm{A}} + \dot{H}_{\mathrm{A,pump}} + T_{\mathrm{A}}\alpha_{\mathrm{A}}V_{\mathrm{A}}\dot{p}_{\mathrm{A}}\right) \tag{43}$$

$$\dot{T}_{\mathrm{B}} = \frac{1}{V_{\mathrm{B}}\rho_{\mathrm{B}}c_{\mathrm{p,B}}}\left(\dot{Q}_{\mathrm{B}} + \dot{H}_{\mathrm{B,pump}} + \dot{H}_{\mathrm{C}}^{-} + T_{\mathrm{B}}\alpha_{\mathrm{B}}V_{\mathrm{B}}\dot{p}_{\mathrm{B}}\right) \tag{44}$$

$$\dot{T}_{\mathrm{C}} = \frac{1}{V_{\mathrm{C}}\rho_{\mathrm{C}}c_{\mathrm{p,C}}}\left(\dot{Q}_{\mathrm{C}} + \dot{H}_{\mathrm{C}}^{+} + \dot{H}_{\mathrm{L,pump}} + T_{\mathrm{C}}\alpha_{\mathrm{C}}V_{\mathrm{C}}\dot{p}_{\mathrm{C}}\right) \tag{45}$$

where $\dot{Q}_{\mathrm{A}}$, $\dot{Q}_{\mathrm{B}}$ and $\dot{Q}_{\mathrm{C}}$ are the sum of heat flows to the control volumes, $\dot{H}_{\mathrm{A,pump}}$, $\dot{H}_{\mathrm{B,pump}}$ and $\dot{H}_{\mathrm{L,pump}}$ are the pump enthalpy flows to the control volumes. $\dot{H}_{\mathrm{C}}^{+}$ and $\dot{H}_{\mathrm{C}}^{-}$ are the enthalpy flow through the orifice. The enthalpy flows are modelled in Section 7.

The *benchmark* model discretises the system into 18 solid thermal capacities each associated with an individual temperature. The temperature dynamics of a solid capacity is modelled as:

$$\dot{T}_j = \frac{\sum_i \dot{Q}_{j,i}}{m_j c_{\mathrm{p},j}} \qquad \dot{Q}_i = \frac{\Delta T_i}{R_{\mathrm{th},i}} \tag{46}$$

where j is indexing the 18 solid capacities and i the heat transfer to the solid capacity. $\sum_i \dot{Q}_{j,i}$ is the net sum of heat flow into capacity j, m_j is the mass of the solid capacity and $c_{\mathrm{p},j}$ is the specific heat for the given solid material modelled as a function of the temperature. Specific heats as a function of temperature are obtained from the library of EES, and implemented as 1D lookup tables. The heat flow is described using the concept of thermal resistances, R_{th}. Analogous to an electric circuit, the temperature (voltage) may be described as the product of heat flow (current) and the thermal resistance [K/W]. $\sum_i \dot{Q}_{j,i}$ is thus the sum of all heat flows through the thermal resistances connected to the capacity, and ΔT_i is the temperature difference across the thermal resistance. The heat flows to oil and solid capacities may be visualised by a thermal resistance network. The resistance network for both the *benchmark* and the *reduced* model are presented in Section 6.

5.2. Reduced Model

The pressure dynamics of the *reduced* model are similar to the dynamics from Equations (40)–(42), except that temperature independent fluid properties, $\tilde{p}, \tilde{\beta}$ and $\tilde{\alpha}$, are utilised. This entails that the temperature coupling term ($\alpha V \dot{T}$) vanishes.

Whereas the *benchmark* model includes 18 solid thermal capacities, the *reduced* model only includes five. These are the electric motor and adapter plate, the cylinder barrel, the manifold, the pump and the accumulator. In Figure 6a, these are illustrated as basic geometries, which are used for heat transfer calculations. These include cubes (blue), horizontal cylinders (green) and spheres (yellow). For comparison, Figure 6b shows 15 of the 18 considered solid thermal capacities approximated as basic geometries used in the *benchmark* model.

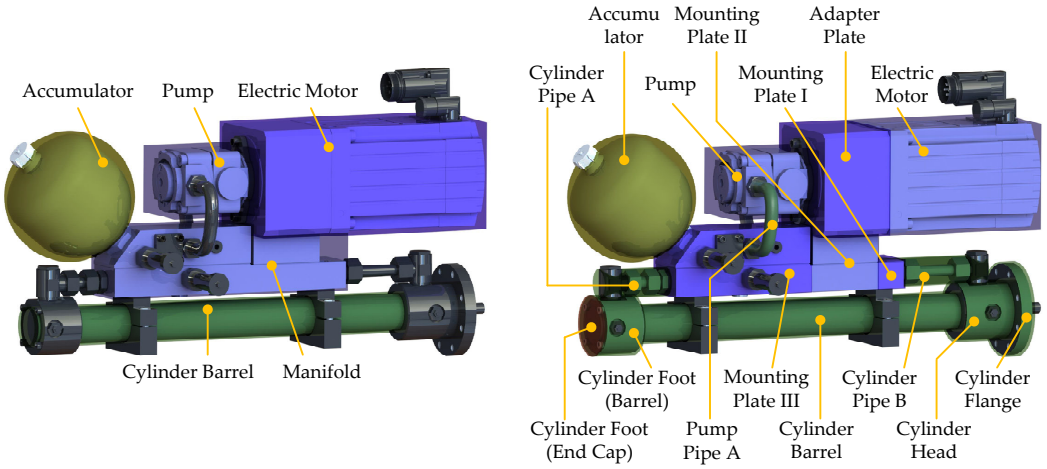

Figure 6. (**a**) In the *reduced* model, natural convection and radiation to the surroundings are modelled to occur from five shapes. (**b**) In the *benchmark* model, natural convection and radiation are modelled to occur from 18 shapes (three not shown).

As noted in [40], the thermal behaviour of the system is governed by the natural convection and radiation resistances on the outer surfaces as these are considerably larger than the forced convection resistances between the oil and the solid materials on the inner surfaces. Taking the cylinder barrel as an example, the combined natural convection and radiation resistance is more than nine times higher than the forced convection resistance. In the *reduced* model, this observation is exploited by neglecting all forced convection resistances, except the forced convection between oil and accumulator, and thus reducing the number of thermal resistances significantly.

This has the implication that all solids being in contact with oil (accumulator not included) are modelled to have the same temperature. This leads to a further simplification compared to the *benchmark* model, as contact and conduction resistances between solid thermal capacities are omitted. However, as a consequence, only three distinct temperatures are modelled in the *reduced* model. These include the oil temperature in the accumulator T_C, the accumulator shell temperature T_{acc} and the lumped system temperature, T_{sys}, combining the thermal capacity of the oil in the A and B chamber with the cylinder barrel, pump, manifold, electric motor and adapter plate capacities. Even though the electric motor and adapter plate are not in contact with the oil, these are included in the lumped system temperature due to large contact areas with the pump and manifold, thus assuming the contact resistance to be small. All other thermal capacities, such as pipes, cylinder flanges, etc., are not included in the *reduced* model. This means that only approximate dimensions of the main system components are needed to parametrise the thermal resistance network.

The temperature dynamics of the three control volumes of the *reduced* model are given as:

$$\dot{T}_{\mathrm{sys}} = \frac{\dot{Q}_{\mathrm{losses}} + \dot{H}_{\mathrm{A,pump}} + \dot{H}_{\mathrm{B,pump}} + \dot{H}_{\mathrm{C}}^{-} - \dot{Q}_{\mathrm{th}}}{V_{\mathrm{A}}\tilde{\rho}_{\mathrm{A}}c_{\mathrm{p,A}} + V_{\mathrm{B}}\tilde{\rho}_{\mathrm{B}}c_{\mathrm{p,B}} + m_{\mathrm{steel}}c_{\mathrm{p,steel}} + m_{\mathrm{alu}}c_{\mathrm{p,alu}}}, \quad \dot{T}_{\mathrm{C}} = \frac{\dot{H}_{\mathrm{L,pump}} + \dot{H}_{\mathrm{C}}^{+} - \dot{Q}_{\mathrm{VII}}}{V_{\mathrm{A}}\tilde{\rho}_{\mathrm{A}}c_{\mathrm{p,A}} + V_{\mathrm{C}}\tilde{\rho}_{\mathrm{C}}} \tag{47}$$

$$\dot{T}_{\mathrm{acc}} = \frac{\dot{Q}_{\mathrm{VII}} - \dot{Q}_{\mathrm{V}}}{m_{\mathrm{acc}}c_{\mathrm{p,acc}}}, \quad \dot{Q}_{\mathrm{losses}} = \dot{Q}_{\mathrm{L,HM}} + \dot{Q}_{\mathrm{L,Cyl}} + \dot{Q}_{\mathrm{L,EM}}, \quad \dot{Q}_{\mathrm{th}} = \dot{Q}_{\mathrm{I}} + \dot{Q}_{\mathrm{II}} + \dot{Q}_{\mathrm{III}} + \dot{Q}_{\mathrm{IV}} + \dot{Q}_{\mathrm{VI}}$$

$\dot{Q}_{\mathrm{I}}$ to $\dot{Q}_{\mathrm{VII}}$ are heat flows through the thermal resistances defined in the next section. m_{steel} and m_{alu} are the mass of steel and aluminium with temperature dependent specific heats $c_{\mathrm{p,steel}}$ and $c_{\mathrm{p,alu}}$, respectively. $\dot{Q}_{\mathrm{L,HM}}$, $\dot{Q}_{\mathrm{L,Cyl}}$ and $\dot{Q}_{\mathrm{L,EM}}$ are hydro-mechanical pump losses, cylinder friction losses and losses of the electric machine, respectively. These are modelled in Section 7 along with the enthalpy flows $\dot{H}$.

6. Thermal Resistance Networks

In this section, the heat flows to the control volumes and the solid capacities for both model complexities are presented. As mentioned, the heat flows are calculated based on the temperature differences across thermal resistances. This may beneficially be visualised using a thermal resistance network. The thermal resistance network for the *benchmark* model was derived in [41] and is shown in Figure 7.

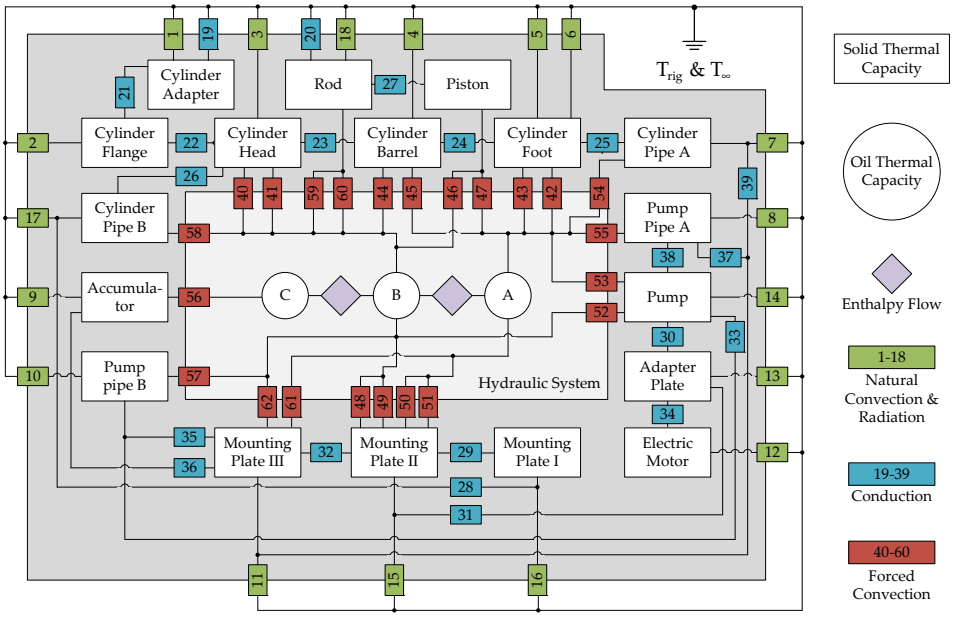

Figure 7. Thermal resistance network for the *benchmark* model. The thermal network was developed in [40,41]. Contact resistance is included in the conduction resistances.

The 62 thermal resistances in Figure 7 were computed in [40,41]. Examples of how to calculate thermal resistances for different geometries and flow conditions are given in Section 6, when calculating resistances for the *reduced* model.

In addition to heat exchanged through thermal resistances, heat is also ascribed as the consequence of energy losses of the components. The power loss due to cylinder friction is entirely added to the cylinder barrel, 25% of the pump friction losses are added to each of the oil control volumes A and B and the remaining 50% are added to the pump housing. Finally, the electric motor power losses are added to the solid capacity of the electric motor. Leakage and valve throttling losses are ascribed inherently by the enthalpy flows.

The thermal resistance network for the *reduced* model is given in Figure 8. In addition to natural convection and radiation from the five basic shapes in Figure 6a, forced convec-

tion between oil and accumulator as well as heat conduction (contact resistance included) from the cylinder barrel through the cylinder head and flange to the test-rig are included.

The seven thermal resistances from Figure 8 are found as either conduction, convection or radiation resistances given as [46]:

$$R_{\text{cond}} = \frac{L}{kA},\ R_{\text{cont}} = \frac{1}{h_c A},\ R_{\text{conv}} = \frac{1}{hA_s},\ R_{\text{rad}} = \frac{1}{A_{s,\text{Eff}}\epsilon\sigma\left(T_s^2 + T_\infty^2\right)(T_s + T_\infty)} \tag{48}$$

where R_{cond} is the conduction resistance (here for a plane wall example) modelling the heat transfer through a material. L is the length of which the heat transfer occurs, k is the thermal conductivity of the material and A is the cross-section area. R_{cont} is the contact resistance, with h_c being the contact conductance. R_{conv} is forced or natural convection resistance. Forced convection occurs between oil and solid elements, whereas natural convection takes place at the outer surfaces of the system, as no fan is incorporated in the system. h is the convective heat transfer coefficient. A_s is the surface area. R_{rad} is radiation resistance, with $A_{s,\text{Eff}}$ being the effective radiation surface area. ϵ is the surface emissivity and σ is the Stefan–Boltzmann constant. T_s and T_∞ are the surface temperature and the ambient temperature, respectively.

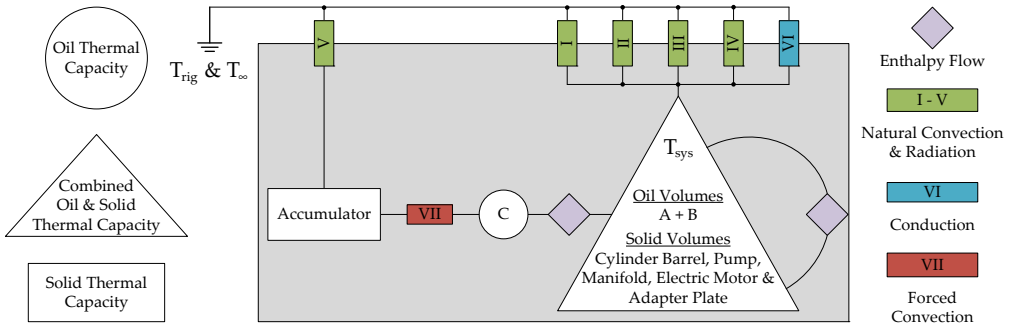

Figure 8. Thermal resistance network for the *reduced* model. The natural convection and radiation resistance are found as a parallel connection of the convection and radiation resistances

6.1. Heat Conduction

Only heat conduction from the cylinder barrel through the cylinder head and flange to the test-rig is included in the *reduced* model. The test-rig is considered as a thermal reservoir, thus remaining at a constant temperature. The heat transfer is modelled as a serial connection of two conduction and two contact resistances (R_{cond} and R_{cont} in Equation (48)). The apparent contact areas for calculation of the contact resistances are given in Figure 9a as A_1 and $(A_1 + A_2)$. The conduction resistances are modelled with areas $(A_1 + A_2)$, $(A_1 + A_2 + A_3)$ and lengths L_1, L_2.

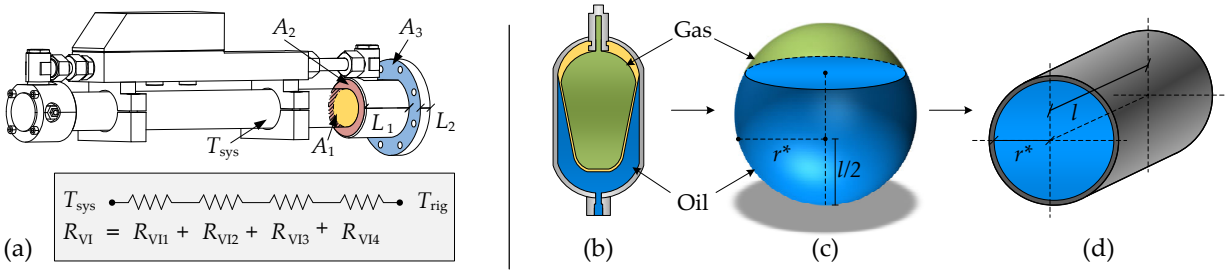

Figure 9. (**a**) The heat conduction from the cylinder barrel to the test-rig is modelled as a serial connection of two conduction and two contact resistances. (**b**) Bladder type gas-loaded accumulator. (**c**) The bladder accumulator is approximated as a sphere when calculating the natural convection heat transfer from the outer surface. (**d**) Forced convection on the inner surface is approximated as internal pipe flow, with the length of the pipe being the oil height in the virtual sphere and the pipe radius being evaluated as the radius of the spherical cap at $l/2$.

6.2. Convection

The convective heat transfer coefficient, h in Equation (48), may be determined from the average Nusselt number (Nu). The Nusselt number is a function of the Reynolds (Re) and Prandtl (Pr) numbers for forced convection problems, and the Rayleigh (Ra) and Prandtl numbers for natural convection problems.

$$\mathrm{Nu}(\mathrm{Re}\,\text{or}\,\mathrm{Ra},\mathrm{Pr}) = \frac{hL_c}{k} \qquad \mathrm{Re} = \frac{\hat{V}L_c\rho}{\mu} \qquad \mathrm{Pr} = \frac{\mu c_p}{k} \qquad \mathrm{Ra} = \frac{g\alpha L_c^3\rho^2 c_p}{\mu k}\Delta T \tag{49}$$

where L_c is the geometry dependent characteristic length, $\hat{V}$ is the mean flow speed and g is the gravitational acceleration. For natural convection problems, the fluid properties of the ambient air are calculated at the reference temperature $\overline{T} = 0.5(T_s + T_\infty)$, i.e., at the mean temperature between surface and surroundings. Fluid properties for forced convection problems are evaluated at the lumped pressure and temperature of the oil control volume using the expressions derived in Section 3.

The Nusselt number depends on geometry, and the methodology utilised here is to identify an appropriate approximation of the considered shape, such that well-known methodologies and formulas valid for basic shapes may be applied. This is done in Figure 6a, where the outer surfaces of the ECD prototype is approximated using the basic shapes of a cube (electric motor and adapter plate, pump and manifold), horizontal cylinder (cylinder barrel) and sphere (accumulator).

To illustrate this approach further, consider the accumulator, which is approximated by a sphere for calculation of the natural convection resistance, as seen in Figure 9b,c. The forced convection between the oil and the accumulator shell is modelled by approximating the flow as an internal pipe flow. The length and diameter of this pipe are updated according to the oil level in the accumulator, which is illustrated in Figure 9c,d. The fluid height present in the virtual sphere is calculated dependent on the oil volume in the accumulator, and is used as the pipe length when calculating the Nusselt number. The pipe diameter is approximated as the diameter of the spherical cap containing the oil at half the oil height, as illustrated in Figure 9c.

Table 2 shows the expressions for calculation of the Nusselt numbers for the geometries and flow conditions considered in the *reduced* model, obtained from [59,60]:

Table 2. Nusselt numbers for convective heat transfer problems in the *reduced* model. A_{proj} is the projected area of the cube on a horizontal flat surface below the cube. d_i is internal diameter. The Nusselt number for internal pipe flow is valid for laminar flows during hydrodynamic and thermal flow development.

	Geometry	Nusselt Number	Prantdl Function	L_c
Natural	Horizontal Cylinder	$\mathrm{Nu} = \left(0.752 + 0.387(\mathrm{Ra}\,f(\mathrm{Pr}))^{1/6}\right)^2$	$f(\mathrm{Pr}) = \left(1 + \left(\frac{0.559}{\mathrm{Pr}}\right)^{9/16}\right)^{-16/9}$	$L_c = \frac{1}{2}\pi d$
	Sphere	$\mathrm{Nu} = 0.56\left(\left(\frac{\mathrm{Pr}}{0.846+\mathrm{Pr}}\right)\mathrm{Ra}\right)^{1/4} + 2$	-	$L_c = d$
	Cube	$\mathrm{Nu} = 5.748 + 0.752\left(\frac{\mathrm{Ra}}{f(\mathrm{Pr})}\right)^{0.252}$	$f(\mathrm{Pr}) = \left(1 + \left(\frac{0.492}{\mathrm{Pr}}\right)^{9/16}\right)^{16/9}$	$L_c = \frac{A}{d}$ $d = \sqrt{4\frac{A_{proj}}{\pi}}$
Forced	Internal Pipe Flow	$\mathrm{Nu} = \left(49.37 + (f_1 - 0.7)^3 + f_2^3\right)^{1/3}$	$f_1 = 1.615\left(\mathrm{RePr}\frac{d_i}{l}\right)^{1/3}$ $f_2 = \left(\frac{2}{1+22\mathrm{Pr}}\right)^{1/6}\left(\mathrm{RePr}\frac{d_i}{l}\right)$	$L_c = d_i$

The heat transfer coefficients for natural convection calculated based on the Nusselt numbers given in Table 2 are valid for idealised conditions. In technical environments such as workshops, factories, etc., the heat transfer coefficients can be assumed to be up

to 20% larger than the theoretical values, according to [61]. This is due to ambient air flow occurring from windows, doors, people walking around, etc. In [41], experiments identified that the ambient conditions caused the natural heat transfer coefficients to be 16% larger than the theoretical values. For a fair comparison between the *benchmark* and *reduced* model, all natural convection heat transfer coefficients used in this paper have been increased by 16% compared to their theoretically obtained counterparts.

6.3. Radiation

All bodies above 0 K emit thermal radiation. However, for the current study, radiation heat transfer is assumed to only occur between the solid elements and the surroundings, and not internally between the solid elements. As seen in Equation (48) the effective radiation surface, $A_{s,Eff}$, is utilised instead of the actual surface area A_s, acknowledging that solid elements may be shadowing each other. This means that the effective radiation area is smaller than the actual surface area. This effect is included in the *benchmark* model, however, the *reduced* model assumes $A_{s,Eff} = A_s$, as the shadowing effect is difficult to determine without accurate knowledge of the relative placement of the solid components.

6.4. Thermal Resistances in the Reduced Model

In Table 3, the seven thermal resistances of the *reduced* model are exemplarily calculated. The resistances have been evaluated at oil and solid temperatures of 60 °C, an ambient temperature of 20 °C, fluid velocities present for a piston speed of 150 mm/s and at the initial oil level in the accumulator. As mentioned, the heat transfer coefficients have been increased by 16% compared to the idealised values to reflect the ambient flow conditions. Please note that the resistances are updated during the simulation, and the values given in Table 3 are only given as an example to illustrate the order of magnitude.

Table 3. Thermal resistances, according to Figure 8, evaluated at oil and solid temperatures of 60 °C, an ambient temperature of 20 °C and for fluid velocities present for a piston speed of 150 mm/s.

Natural Convection & Radiation									
ID	Geometry	A_s	A_{proj}	L_c	ϵ	h_{conv}	h_{rad}	h_{comb}	R_{th}
I	Horizontal Cylinder	980 cm^2	-	79 mm	0.92	7.1 $\frac{W}{m^2K}$	6.4 $\frac{W}{m^2K}$	13.5 $\frac{W}{m^2K}$	0.76 $\frac{K}{W}$
II	Cube (Manifold)	1341 cm^2	221 cm^2	799 mm	0.26	5.0 $\frac{W}{m^2K}$	1.8 $\frac{W}{m^2K}$	6.8 $\frac{W}{m^2K}$	1.1 $\frac{K}{W}$
III	Cube (Electric Motor)	2268 cm^2	469 cm^2	928 mm	0.69	4.8 $\frac{W}{m^2K}$	4.8 $\frac{W}{m^2K}$	9.6 $\frac{W}{m^2K}$	0.46 $\frac{K}{W}$
IV	Cube (Pump)	614 cm^2	120 cm^2	497 mm	0.92	5.7 $\frac{W}{m^2K}$	6.4 $\frac{W}{m^2K}$	12.1 $\frac{W}{m^2K}$	1.34 $\frac{K}{W}$
V	Sphere (Accumulator)	707 cm^2	-	150 mm	0.92	5.9 $\frac{W}{m^2K}$	6.4 $\frac{W}{m^2K}$	12.4 $\frac{W}{m^2K}$	1.14 $\frac{K}{W}$
Heat Conduction to Test-Rig									
ID	Geometry	A_1	A_2	A_3	L_1	L_2	k [46]	h_c [40]	R_{th}
VI	Plane Wall	20 cm^2	28 cm^2	75 cm^2	73 mm	16 mm	63.9 $\frac{W}{mK}$	6.5 $\frac{kW}{m^2K}$	0.37 $\frac{K}{W}$
Forced Convection (Oil to Accumulator)									
ID	Geometry	A_s	l	d_i	$\hat{V}$		Re	h_{conv}	R_{conv}
VII	Internal Pipe Flow	243 cm^2	51.6 mm	113 mm	7.6 $\frac{mm}{s}$		28	51 $\frac{W}{m^2K}$	0.80 $\frac{K}{W}$

The simple thermal resistance network and the associated numerical values of the resistances given in Table 3 enable performing some rough estimations of the static thermal behaviour of the system. From Figure 8, the equivalent thermal resistance to the surroundings from the lumped system components, at T_{sys}, is 0.120 K/W (assuming $T_C = T_{sys}$). If the average losses of the ECD are 450 W, this yields a static system temperature of 54 °C above the ambient temperature. Note that this is a rough estimate as the thermal resistances in Table 2 are temperature dependent themselves.

In [41], one of the main conclusions was that the modelled temperature was sensitive towards estimation errors of the power losses. The equivalent thermal resistance of 0.12 K/W may also be used to approximate the sensitivity towards estimation errors of the energy losses of the system or the thermal resistances. Assume the average losses to be estimated within ± 20%. This would result in estimated static temperatures in the range from 43 °C to 65 °C above ambient temperature, showing a relatively large sensitivity towards power loss estimating errors.

Furthermore, Table 3 shows that the surface area weighted mean of the combined heat transfer coefficients for natural convection and radiation is 10.2 $\frac{W}{m^2K}$. Note, if the theoretical natural heat transfer coefficients are used this number would equal 9.5 $\frac{W}{m^2K}$. Assuming this to be the only heat transfer occurring in the system, i.e., neglecting forced convection and conduction, this may be used as an approximate number, in the early design phase of an ECD to assess if special attention is required for the thermal design. As such it may be possible for a design engineer to roughly estimate the static thermal behaviour of the ECD, if an estimate of the system losses and the outer surface area can be established.

7. Component Models

As the last step before the simulation results are presented, the component models of the cylinder, pump and orifice are presented. These are common for both the *benchmark* and the *reduced* model and are needed to quantify the losses of the ECD and to define the mass and enthalpy flows used in the dynamic equations. The hydraulic diagram including the components as well as mass and enthalpy flow names are repeated in Figure 10a for convenience.

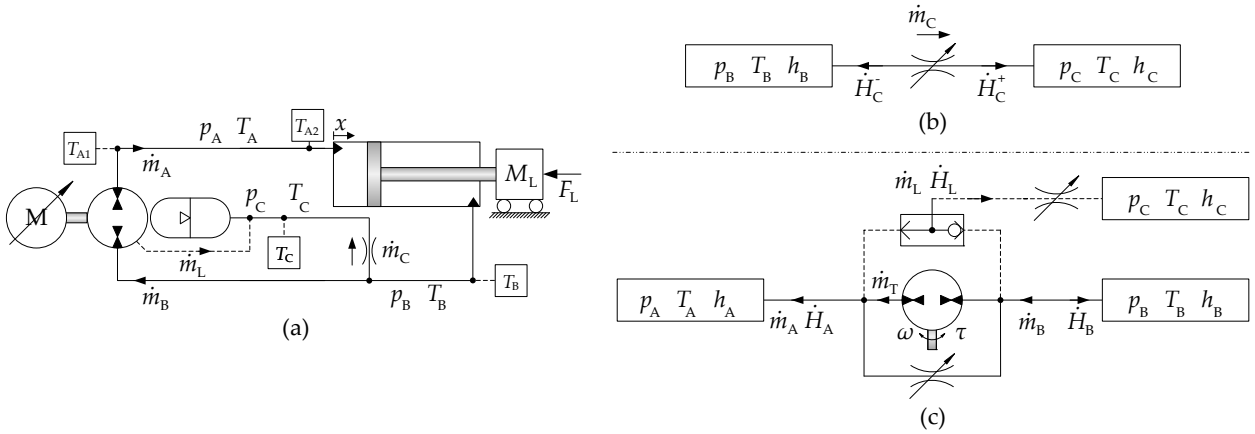

Figure 10. (**a**) Simplified schematic valid for the conducted experiments. (**b**) Simple schematic showing the quantities used for modelling mass and enthalpy flow of the inverse shuttle valve/orifice. (**c**) The inputs to the static pump model are the fluid properties in the adjacent chambers, and the shaft speed ω. The shaft torque as well as mass and enthalpy flows are model outputs.

7.1. Cylinder and Orifice

Equation (50) expresses the motion dynamics and the friction losses of the cylinder.

$$\ddot{x} = \frac{1}{M_L}(p_A A_A - p_B A_B - (A_A - A_B)p_0 - F_L - F_F) \qquad \dot{Q}_{L,Cyl} = F_F \dot{x} \tag{50}$$

$$F_F = \left(F_c + (F_s - F_c)e^{\frac{-|\dot{x}|}{\dot{x}_{sw}}} + K_p|p_A - p_B|\right)\tanh(\gamma\dot{x}) + B_L\dot{x} \tag{51}$$

The term $(A_A - A_B)p_0$ includes the force from the surroundings on the rod and is included because the modelled pressures are absolute. F_L is the load force and F_F is cylinder friction modelled as a Stribeck characteristic curve including a pressure dependent friction term [62,63]. F_c is the Coulomb friction, F_s is the static friction, $\dot{x}_{sw}$ is the Stribeck velocity, K_p is the pressure dependent friction coefficient and B_L is the viscous friction coefficient.

The mass and enthalpy flows of the inverse shuttle valve/orifice are modelled according to Figure 10b as [52]:

$$\dot{m}_C = A_o C_d \sqrt{2\overline{\rho}|p_B - p_C|}\ \mathrm{sign}(p_B - p_C) \tag{52}$$

$$\dot{H}_C^+ = \begin{cases} \dot{m}_C(h_B - h_C) & , \ \dot{m}_C \geq 0 \\ 0 & , \ \dot{m}_C < 0 \end{cases} \qquad \dot{H}_C^- = \begin{cases} 0 & , \ \dot{m}_C \geq 0 \\ -\dot{m}_C(h_C - h_B) & , \ \dot{m}_C < 0 \end{cases} \tag{53}$$

where A_0 is the orifice area and C_d is the discharge coefficient.

7.2. Electric Motor

The dynamics of the electric motor is omitted in the model, i.e., the shaft speed equals the reference speed. Thus, only the loss behaviour of the motor is modelled. The losses of the electric motor are measured for varying motor speeds and torques and implemented as a 2D lookup table. The losses are assumed to be temperature independent and identical in both generator and motor operation mode. For a visualisation of the loss behaviour of the motor, the measured efficiency map is shown in Figure 11a.

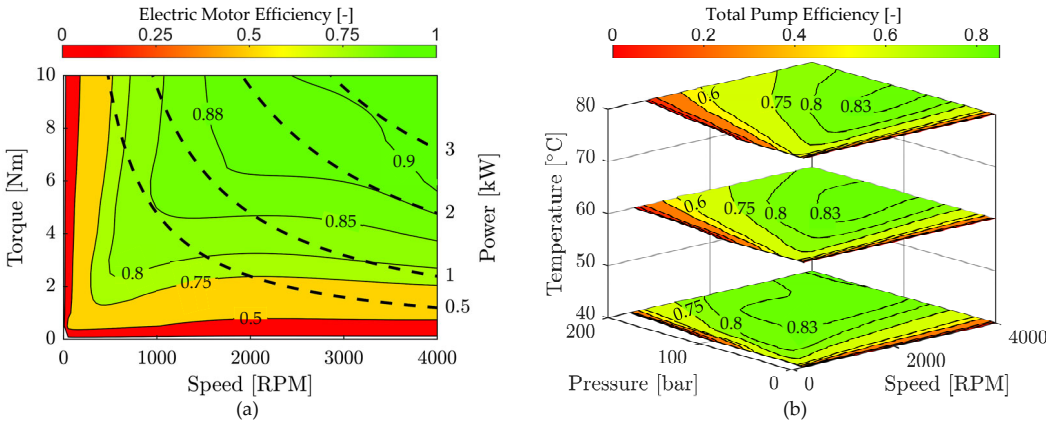

Figure 11. (**a**) Measured efficiency map of the electric motor, as a function of torque and speed. Dotted lines are power levels. (**b**) Measured efficiency map of the pump as a function of pressure difference, speed and temperature.

7.3. Pump

A pump model expressing the static relationship between the inputs (i.e., the pump speed, pressure difference across the pump and inlet temperature) and the outputs is needed. The outputs include the mass and enthalpy flows as well as the shaft torque. This is visualised in Figure 10c. Here, it may also be seen that external leakage is modelled to only occur from the high pressure chamber.

In addition to the mentioned model inputs, loss information or loss models are required, which may either be an analytical model or simply measured loss quantities, implemented as look-up tables. The latter approach is used here. Figure 11b shows the measured efficiency map of the pump. Losses are assumed to be equivalent in both motor and pump operation modes. The actual pumping process is modelled as an ideal process, with losses/irreversibilities added subsequently. E.g., leakage losses may be regarded as variable orifices surrounding the ideal pump process (as visualised in Figure 10c). From Figure 10c, it is important to note that the inlet pressure and temperature to the ideal pump equal the states of the delivering chamber (rotation direction dependent), and the outlet pressure equals the pressure in the receiving chamber. The output temperature, however, is calculated by assuming an isentropic compression process, as [47]:

$$S = f(T,p) \quad \Rightarrow \quad dS = \left(\frac{\partial S}{\partial T}\right)_{\mathrm{p}} dT + \left(\frac{\partial S}{\partial p}\right)_{\mathrm{T}} dp = \frac{c_{\mathrm{p}}}{T} dT - \alpha v dp \tag{54}$$

$$\xrightarrow{dS=0} \quad dT = \frac{\alpha T}{\rho c_{\mathrm{p}}} dp \quad \xrightarrow{\text{Approximation}} \quad T_{\mathrm{out}} \cong T_{\mathrm{in}} + \frac{\overline{\alpha} T_{\mathrm{in}}}{\overline{c}_{\mathrm{p}} \overline{\rho}} (p_{\mathrm{out}} - p_{\mathrm{in}}) \tag{55}$$

S is the entropy modelled as a function of temperature and pressure, p_{in} and p_{out} is either p_{A} or p_{B} depending on the direction of rotation. Likewise, the inlet temperature is either T_{A} or T_{B}. $\overline{\bullet}$ denotes fluid properties evaluated at $\frac{p_{\mathrm{in}}+p_{\mathrm{out}}}{2}$ and T_{in}. The enthalpy change of the fluid may be found by inserting the isentropic temperature change from Equation (55) in Equation (19):

$$dh = c_{\mathrm{p}} dT + v(1 - T\alpha) dp = c_{\mathrm{p}} \left(\frac{\alpha T}{\rho c_{\mathrm{p}}} dp\right) + v(1 - T\alpha) dp = \frac{1}{\rho} dp \tag{56}$$

$$\xrightarrow{\text{Approximation}} \quad \Delta h \cong \frac{1}{\overline{\rho}} (p_{\mathrm{out}} - p_{\mathrm{in}}) \tag{57}$$

where $\overline{\rho}$ is the fluid density evaluated at $\frac{p_{\mathrm{in}}+p_{\mathrm{out}}}{2}$ and $\frac{T_{\mathrm{in}}+T_{\mathrm{out}}}{2}$. The ideal mass flow, $\dot{m}_{\mathrm{T}}$, the mass leakage flow, $\dot{m}_{\mathrm{L}}$ and the theoretical pump torque are modelled as:

$$\dot{m}_{\mathrm{T}} = \omega D_{\mathrm{p}} \overline{\rho} \qquad \dot{m}_{\mathrm{L}} = \frac{1}{2} Q_{\mathrm{L}} \overline{\rho} \qquad \tau_{\mathrm{T}} \omega = \dot{m}_{\mathrm{T}} \Delta h \quad \Rightarrow \quad \tau_{\mathrm{T}} = D_{\mathrm{p}} (p_{\mathrm{out}} - p_{\mathrm{in}}) \tag{58}$$

where D_{p} is the geometric displacement of the pump and Q_{L} is the measured volumetric flow loss. Note that τ_{T} ends up being the familiar torque equation for incompressible fluids. To include the compressibility of the fluid, somewhat more elaborate models are available, i.e., from [64], but are not considered here. The calculation of the mass and enthalpy flows, defined in Figure 10c, depend on the operating quadrant, i.e., the direction of pump rotation and the pressure difference across the pump. Likewise, the actual shaft torque τ must be calculated based on the operation quadrant by including the measured torque loss τ_{L}.

The relevant expressions for the four operating quadrants are given in Table 4:

Table 4. Pump torque, mass and enthalpy flows based on operation quadrant. $\Delta P = (p_A - p_B)$. * Only valid for $\dot{m}_A > 0$, † Only valid for $\dot{m}_B < 0$.

		Pump Model Outputs					
	Quadrant	τ	$\dot{m}_A$	$\dot{m}_B$	$\dot{H}_A$	$\dot{H}_B$	$\dot{H}_L$
I	$(\omega \geq 0)$ $(\Delta P \geq 0)$	$\tau_T + \tau_L$	$\dot{m}_T - 2\dot{m}_L$	$\dot{m}_T - \dot{m}_L$	$\dot{m}_A(h_B + \Delta h - h_A)^{\star}$	$\dot{m}_L \Delta h^{\star}$	$\dot{m}_L(h_B + \Delta h - h_C)^{\star}$
II	$(\omega < 0)$ $(\Delta P > 0)$	$-\tau_T - \tau_L$	$\dot{m}_T - 2\dot{m}_L$	$\dot{m}_T - \dot{m}_L$	0	$\dot{m}_L(h_A - h_B) - \dot{m}_T(h_A + \Delta h - h_B)$	$\dot{m}_L(h_A - h_C)$
III	$(\omega < 0)$ $(\Delta P < 0)$	$-\tau_T - \tau_L$	$\dot{m}_T + \dot{m}_L$	$\dot{m}_T + 2\dot{m}_L$	$\dot{m}_L \Delta h^{\dagger}$	$-\dot{m}_B(h_A + \Delta h - h_B)^{\dagger}$	$\dot{m}_L(h_A + \Delta h - h_C)^{\dagger}$
IV	$(\omega > 0)$ $(\Delta P < 0)$	$\tau_T + \tau_L$	$\dot{m}_T + \dot{m}_L$	$\dot{m}_T + 2\dot{m}_L$	$\dot{m}_L(h_B - h_A) - \dot{m}_T(h_B + \Delta h - h_A)$	0	$\dot{m}_L(h_B - h_C)$

8. Results

The ECD prototype presented in Section 4 was tested in the laboratory by controlling it to follow a sinusoidal position reference with a frequency of 0.4 Hz (t_{cycle} = 2.5 s), reaching maximum cylinder and motor speeds of ±300 mm/s and ±3600 RPM, respectively. A constant load force of 5 kN is requested by the load cylinder, but due to friction and load dynamics, this is found to be varying between 3.9 kN and 5.7 kN. The test continued for a period of three hours until thermal equilibrium was reached. Oil temperatures were measured using four thermocouples (see position in Figure 10a) with an accuracy of ±0.5 K. The surface temperatures of the prototype were monitored by a thermo-graphic camera having an accuracy of ± 1.5 K. The measured load force and the position reference were used as the simulation inputs. The derived governing equations were simulated in MatLAB Simulink using the ODE45-solver, with a maximum stepsize of 1/5000 s. Using a laptop with an Intel i7-10610 1.8 GHz processor, a 10 min simulation of the *benchmark* model was completed within 20 min, whereas the simulation of the *reduced* model was completed within 13 min.

8.1. Loss Behaviour

As illustrated in the previous section, the modelled temperature is rather sensitive towards inaccuracies between actual and modelled heat losses. Therefore, the simulated and measured loss behaviour is compared in Figure 12.

Figure 12b,d,f show a good coherence between the measured and simulated pressure in all control volumes. For the pressure in the piston chamber (p_A), the oscillation frequency is modelled fairly accurately while the measured damping is slightly larger than the modelled damping. Interestingly, it is found that there are no noticeable differences between the pressures modelled in the *benchmark* and the *reduced* models, even though the dynamic pressure–temperature coupling is neglected in the *reduced* model.

No noticeable differences are found between the two model complexities for any of the quantities visualised in Figure 12, expect for the accumulator pressure. Here small deviations of approximately 0.05 bar can be seen.

Figure 12a shows a good coherence between the measured and simulated position. Combined with the accurately modelled chamber pressures, this leads to the cylinder power being modelled accurately, as seen in Figure 12c.

Slight deviations exist between the modelled and estimated shaft torque and power during cylinder retraction, at ∼2 s and ∼4.5 s in Figure 12e. On average, it is found that the input power to the hydraulic system and the output power are modelled with an acceptable accuracy. This means that the losses are established with a sufficient degree of accuracy for anticipating the thermal behaviour. In other words, deviations between modelled and simulated temperatures are assessed to originate from inaccurate heat transfer models rather than loss model deviations.

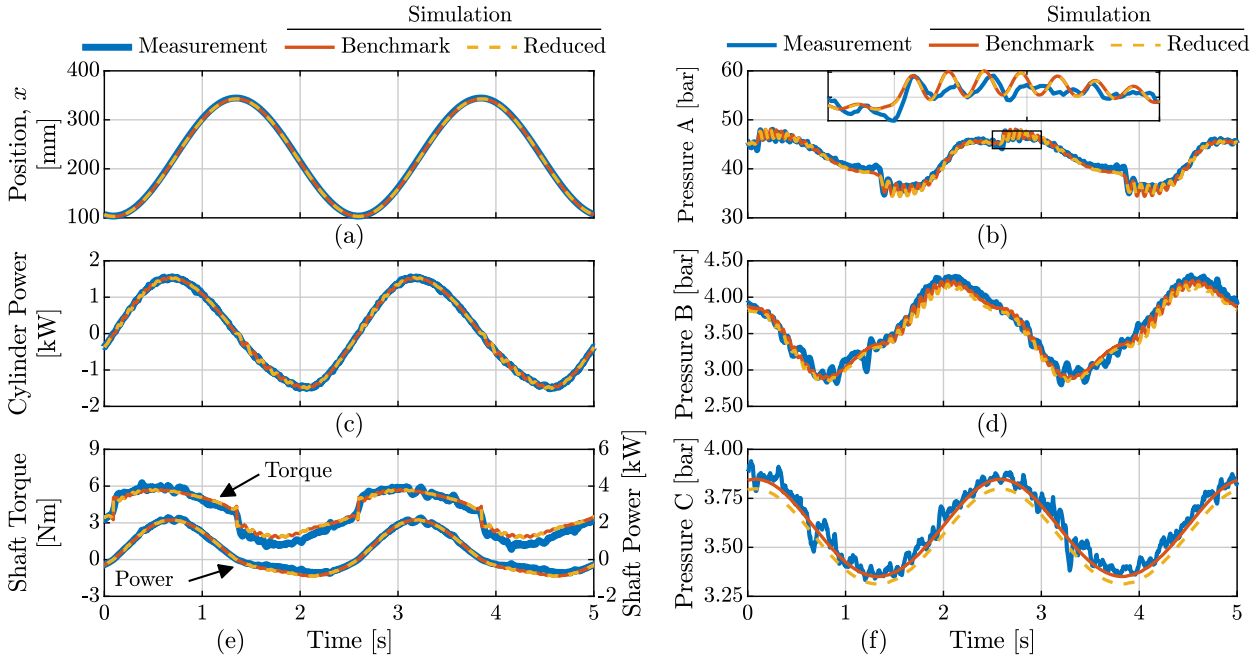

Figure 12. (**a**) Measured and simulated piston position. (**b**) Measured and simulated pressure in the piston chamber p_A. (**c**) Measured and simulated mechanical output power ($\dot{W} = \dot{x}F_{cyl}$). (**d**) Measured and simulated pressure in the rod chamber p_B. (**e**) Measured and simulated shaft torque and shaft power ($\dot{W} = \omega\tau$). (**f**) Measured and simulated accumulator pressure.

8.2. Static Temperatures

Even though the derived models are dynamic models, the transient temperature development is not important in some applications. If a system is going to perform the same task 24 h a day for 20 years, it is not important if static temperatures are reached after 10 min or 10 h. In this situation, only the static temperatures are relevant to ensure that the oil temperature stays within limits.

Figure 13a compares the *benchmark* modelled oil and surface temperatures with the measured values. Regarding the surface temperatures, the high number of simulated thermal capacities in the *benchmark* model pays off in terms of the ability to fairly accurately model the qualitative temperature distribution, e.g., the model predicts that the motor is warmer than the pump and that the cylinder head is colder than the cylinder barrel. This information is lost in the *reduced* model due to the simplification of only including three thermal capacities. As seen in Figure 13b, only two different surface temperatures are modelled, i.e., the surface temperature of the accumulator and the lumped temperature of the remaining system.

The *benchmark* model in Figure 13a models all surface temperatures within ± 5.5 K. Furthermore the oil temperatures are estimated within approximately ± 1.5 K, except for the oil temperature in the rod side chamber, which is overestimated with approximately 3 K. This is assessed to be satisfactorily accurate for analysis purposes, e.g., to analyse the effect of changing certain parameters such as areas and emissivities on the thermal behaviour.

As mentioned, the *reduced* model in Figure 13b is not formulated such that it is capable of predicting the individual temperature distribution of the system. This is because all system components, except the accumulator, are lumped in a single thermal capacity. This was chosen to avoid parametrising a high number of forced convection and conduction resistances. The modelled surface temperature of the system components are somewhat in-between the highest system temperature of the motor and the lowest system temperature of the cylinder barrel. Given the reduced complexity of the model, this is the expected result, but it leads to deviations up to 6.4 K, considering the surface temperatures.

In terms of the modelled oil temperatures in the *reduced* model, these are overestimated by 1.4 K to 6.8 K. However, all modelled oil temperatures are larger than the measured, meaning that the simulated temperatures are conservative estimates, which is desired in terms of design tool applicability. For comparison, it can be noted that if the natural convection resistances have not been corrected for the ambient flow conditions, i.e., the idealised values are used, the modelled temperatures would be approximately 2 K larger, than the ones given in Figure 13b.

A trade-off between modelling complexity and accuracy is identified in the comparison between the *benchmark* and the *reduced* model. Due to the simple thermal network, which may be parametrised relatively easy, this is much more applicable in the design phase, compared to the *benchmark* model. Furthermore, the *reduced* model produces reasonably accurate and conservative temperature estimates, which may be valuable to have available in the design phase. In this manner, important choices related to the thermal design of the system can be made on a fairly informed basis.

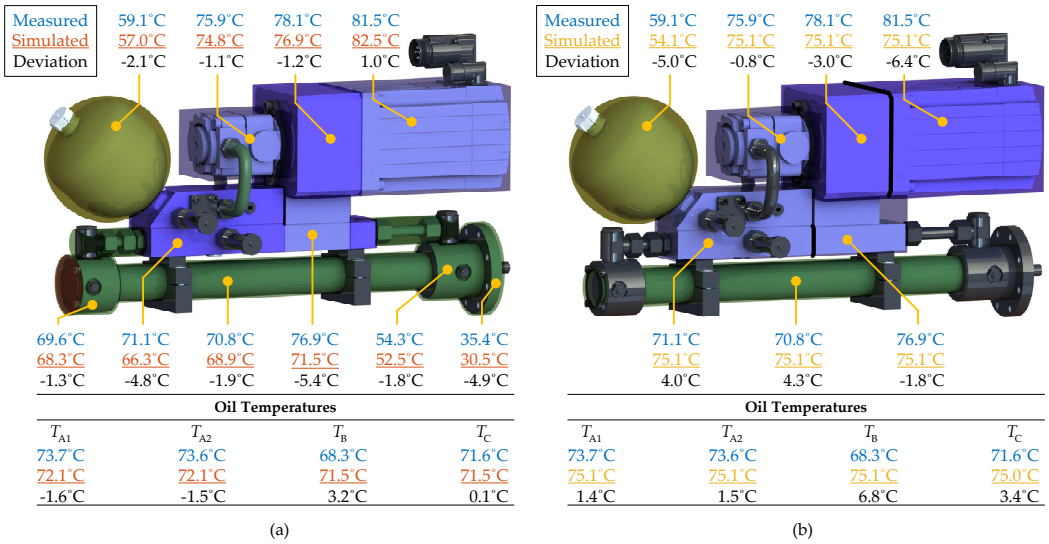

Figure 13. (**a**) Simulated steady state temperatures of the *benchmark* model compared to the measured static temperatures of the ECD prototype. (**b**) Simulated steady state temperatures of the *reduced* model compared to the measured static temperatures of the ECD prototype.

8.3. Transient Temperature

In applications where actuators are used on an on/off basis, i.e., the actuator is working for a limited time with cooling breaks in between the operating cycles, transient temperature behaviour may be relevant to optimise the thermal design. Figure 14 compares the simulated transient temperature responses of the two model complexities and the measurements.

A general thing to observe from Figure 14 is that the *benchmark* model for most of the thermal capacities predicts the transient temperature more accurately than the *reduced* model. The *reduced* model heats up too slowly during the first 45 min, which can be explained by all system components being lumped together. This means that the transient temperature response is governed by the components with large heat capacities. In this case, this is the motor and the mounting plates (Figure 14d,f,g). A reasonably transient fit is seen for these components in the *reduced* model.

To illustrate how neglecting the dynamic pressure–temperature coupling in the *reduced* model influences the transient temperature, consider Figure 14a, where the oil temperature in the piston chamber, T_A, is shown. In the *benchmark* model, temperature oscillations of ∼0.2 K are seen, and is due to pressure oscillations and the dynamic coupling by the thermal expansion coefficient α. In the *reduced* model, the same pressure oscillations are present, as shown in Figure 12b, but this does not result in any temperature oscillations,

as the dynamic coupling is neglected. The temperature oscillations of the *benchmark* model are, however, insignificant with respect to the dominating dynamics; thus, it is found that neglecting the dynamic coupling i.e., defining $\tilde{\alpha} = 0$ is recommendable, as it enables a decoupled simulation of pressure and temperature dynamics.

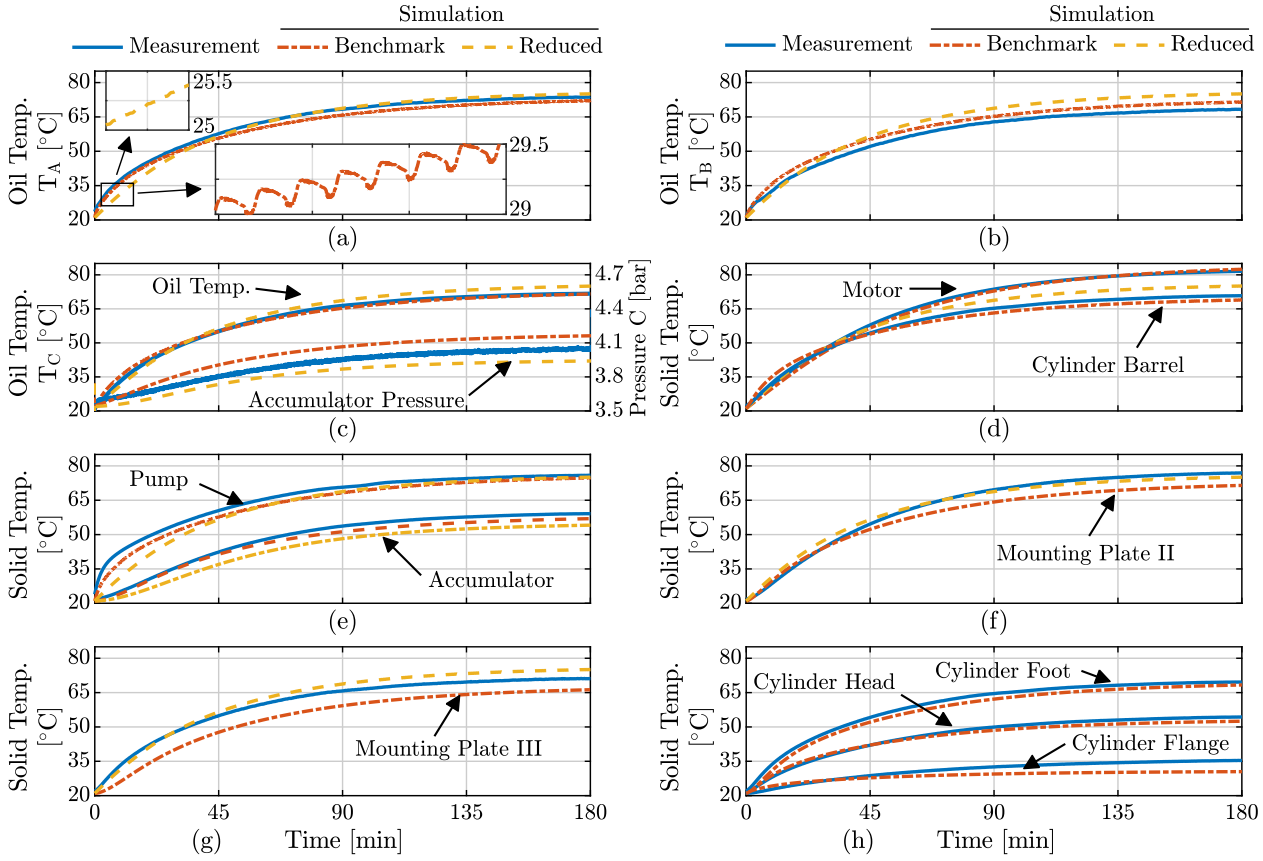

Figure 14. (**a**) Measured and simulated oil temperature in the piston chamber T_A. (**b**) Measured and simulated oil temperature in the rod chamber T_B. (**c**) Measured and simulated oil temperature and pressure in the accumulator T_C and p_C. (**d**) Measured and simulated surface temperatures of the motor and cylinder barrel. (**e**) Measured and simulated surface temperatures of the pump and accumulator shell. (**f**) Measured and simulated surface temperatures of mounting plate II. (**g**) Measured and simulated surface temperatures of mounting plate III. (**h**) Measured and simulated surface temperatures of the cylinder head, flange and foot. This is only available for the *benchmark* model, as these components are not included in the *reduced* model.

Another difference arising as a result of neglecting the pressure–temperature coupling is visible in Figure 14c, where the average accumulator pressure for one operating cycle is plotted. As the thermal expansion of the oil is defined as zero in the *reduced* model, the accumulator pressure only increases due to thermal expansion of the gas in the accumulator. For the *benchmark* model, the accumulator must contain a larger oil volume as the oil temperatures increase, resulting in a higher pressure compared to the *reduced* model. However, both model complexities predicts the measured pressure within ± 0.15 bar, which is fairly accurate.

To sum up the presentation of the modelling results, it is found that there is a trade-off in terms of accuracy and thermal modelling complexity. Both model complexities, however, predict the temperature with an accuracy found to be reasonable for design purposes. Note that this is partly possible because the losses of the ECD prototype was modelled with a high degree of accuracy. For most applications, the relatively small differences in terms of modelled temperatures cannot justify the formulation of the elaborate thermal network of the *benchmark* model compared with the *reduced* model. Note that the number of resistances

are reduced from 62 in the *benchmark* model to 7 in the *reduced* model. More importantly the seven resistances can be parametrised fully based on cylinder, motor, accumulator and manifold dimensions. These are available with some accuracy in the design phase of the system, thus making the *reduced* modelling framework a valuable tool for proper thermal design. To fully utilise the framework as a design tool, the modelling accuracy when including various heat transfer enhancing designs must be investigated. This may be the effect of including a fan, an oil cooler, heat pipes in the manifold or even a water cooled manifold.

9. Conclusions

In this paper, a lumped thermo-hydraulic model for electro-hydraulic compact drives (ECDs) was derived and experimentally verified. To investigate the trade-off between accuracy and modelling complexity, the paper presents two model complexities. It is found that neglecting the dynamic pressure–temperature coupling does not affect the main pressure and temperature dynamics significantly. Therefore, it is recommended to neglect this coupling as it simplifies model development. Additionally, it is found that an elaborate thermal resistance network predicts the oil and surface temperatures of an ECD prototype slightly more accurately than a significantly simplified model structure. For most applications, the small differences in terms of modelled temperatures cannot justify the formulation of the elaborate thermal network compared to the simplified network. The findings in the paper may lead to the acceptance of simplified thermo-hydraulic model structures that are applicable in the early design phase where only limited information about the system is available. This may be an important contribution toward proper thermal design of ECDs needed to expand the application range of the technology.

Author Contributions: Conceptualization: S.K., S.M. and L.S.; methodology: S.K., S.M. and L.S.; software: S.K.; experimental work: S.M.; data analysis: S.K. and S.M.; writing—original draft preparation: S.K.; review: S.M., L.S. and M.K.E.; editing: S.K.; supervision; L.S., M.K.E., T.O.A. and J.W.; project administration: M.K.E. and T.O.A.; funding acquisition: M.K.E. and T.O.A. All authors have read and agreed to the published version of the manuscript.

Funding: This research was funded by the Research Council of Norway, SFI Offshore Mechatronics, project number 237896/O30.

Institutional Review Board Statement: Not applicable.

Informed Consent Statement: Not applicable.

Data Availability Statement: Not applicable.

Conflicts of Interest: The authors declare no conflict of interest.

Abbreviations

The following abbreviations are used in this manuscript:

CFD	Computational Fluid Dynamics
CV	Control Volume
ISV	Inverse Shuttle Valve
RPM	Revolutions per Minute
CS	Control Surface
ECD	Electro-Hydraulic Compact Drives
MBW	Moving Boundary Work

Appendix A. Nomenclature

Symbol	Description	Unit	Symbol	Description	Unit
α	Isobaric expansion coefficient	K^{-1}	$\dot{H}$	Enthalpy Flow	W
β,β_{eff}, β_{mech}	Isothermal, Effective and Mechanical	Pa	k	Thermal Conductivity	W/mK
	Bulk Modulus		L_c	Characteristic Length	m
ϵ	Emissivity	-	$\dot{m}$	Mass Flow	
μ	Dynamic Viscosity	Ns/m^2	$\hat{\mathbf{n}}$	Normal Vector	
ν	Specific Volume	m^3/kg	p	Pressure	Pa
ρ, ρ_A, ρ_F	Mixture, Air, Oil density	kg/m^3	$\dot{Q}$	Heat Flow	W
ω	Shaft Speed	rad/s	R_{th}	Thermal Resistance	K/W
τ,τ_L,τ_T	Shaft Torque, Torque Losses,	Nm	S	Entropy	J/K
	Theoretical Torque		T_s,T	(Surface) Temperature	K
$\bar{\bullet}$	Property evaluated at average conditions		u	Specific Internal Energy	J/kg
$\tilde{\bullet}$	Temperature Indepedent Property		U	Internal Energy	J
$\bullet_A$,$\bullet_B$,$\bullet_C$	Quantify evaluated in CV A, B or C		$\hat{V}$,$\hat{\mathbf{V}}$	Fluid Speed & Velocity Vector	m/s
A, A_s	Area & Surface Area	m^2	V, V_x	Volume & Volume at p_0	m^3
c_p, c_v	Isobaric & Isochoric Specific Heat	J/kgK	$\dot{W}$	Rate of Work	W
d, d_i	Diameter, Internal Diameter	m	x	Piston Position	m
F_L, F_F	Load & Cylinder Friction Force	N	z	Height in Gravitational Field	m
h	Convection Heat Transfer Coefficient	W/m^2K			
h	Specific Enthalpy	J/kg			

Appendix B. Modelling Parameters

Symbol	Description	Value	Symbol	Description	Value
α_0	Expansion Coefficient at p_0, T_0	0.00067 K^{-1}	B_L	Cylinder Viscous Friction	285 Ns/m
β_0	Bulk Modulus at p_0, T_0	1.65 GPa	C_d	Orifice Discharge Coefficient	0.7
β_{mech}	Mechanical Bulk Modulus	0.3 GPa	c_{p0}	Oil Specific Heat Parameter	657 J/kgK
ϵ	Volumetric Air Ratio	0.01	D_p	Pump Displacement	6.3 cm^3/rev
κ	Polytropic process coefficient	1.4	F_s	Static Friction	90 N
ρ_{F0}	Oil Density at p_0, T_0	873 kg/m^3	F_c	Coulomb Friction	15 N
σ	Stefan-Boltzmann Constant		g	Gravitational Acceleration	9.82 m/s^2
τ	Thermal Time Constant	3.5 s			
A_A	Cylinder Piston Area	12 cm^2	K_{cp}	Oil Specific Heat Parameter	4.21 J/kgK^2
A_B	Rod Chamber Area	8.8 cm^2	K_P	Friction Parameter	0.9 N/bar
A_o	Orifice Area	14 mm^2	M_L	Load Mass	112.5 kg

Modelling Parameters Continued					
Symbol	**Description**	**Value**	**Symbol**	**Description**	**Value**
a_{k1}	Conductivity Parameter	0.17 W/mK	p_0	Atmospheric Pressure	1.01 bar
a_{k2}	Conductivity Parameter	97 μW/mK^2	p_{acc0}	Precharge Pressure	2.4 bar
$a_{\mu 1}$	Viscosity Model Parameter	63 Ns/mm^2 bar	R	Air Gas Constant	287 J/kgK
$a_{\mu 2}$	Viscosity Model Parameter	880K	T_0	Reference Temperature	288.15 K
$a_{\mu 3}$	Viscosity Model Parameter	178K	T_{acc0}	Precharge Temperature	288.15 K
$a_{\mu 4}$	Viscosity Model Parameter	334 bar	T_{rig},T_{inf}	Test-rig & Ambient Temp.	296.15 K
$a_{\mu 5}$	Viscosity Model Parameter	3.26 bar/K	V_{acc}	Volume of Accumulator	1.4 L

References

1. Michel, S.; Weber, J. Energy-efficient Electrohydraulic Compact Drives for Low Power Applications. In Proceedings of the ASME/BATH Symposium on Fluid Power & Motion Control, Bath, UK, 12–14 September 2012.
2. Wiens, T.; Deibert, B. A low-cost miniature electrohydrostatic actuator system. *Actuators* **2020**, *9*, 1–16, doi:10.3390/act9040130.
3. Fassbender, D.; Minav, T Finding the Perfect Match: Different Heavy-Duty Mobile Applications Call for Different Actuators. In Proceedings of the 1st International Electronic Conference on Actuator Technology (IeCAT 2020), Online, 23–27 November 2020.
4. Costa, G.K.; Sepehri, N. Four-Quadrant Analysis and System Design for Single-Rod Hydrostatic Actuators. *J. Dyn. Syst. Meas. Control* **2018**, *141*, doi:10.1115/1.4041382.
5. Costa, G.K. A Critical Analysis of Valve-Compensated Hydrostatic Actuators: Qualitative Investigation. *Actuators* **2019**, *8*, doi:10.3390/act8030059.
6. Gøytil, P.H.; Padovani, D.; Hansen, M.R. A novel solution for the elimination of mode switching in pump-controlled single-rod cylinders. *Actuators* **2020**, *9*, doi:10.3390/act9010020.
7. Imam, A.; Rafiq, M.; Jalayeri, E.; Sepehri, N. A Pump-Controlled Circuit for Single-Rod Cylinders that Incorporates Limited Throttling Compensating Valves. *Actuators* **2018**, *7*, 13, doi:10.3390/act7020013.
8. Çalışkan, H.; Balkan, T.; Platin, B.E. A Complete Analysis and a Novel Solution for Instability in Pump Controlled Asymmetric Actuators. *J. Dyn. Syst. Meas. Control* **2015**, *137*, 091008, doi:10.1115/1.4030544.
9. Minav, T.; Panu, S.; Matti, P. Direct-Driven Hydraulic Drive Without Conventional Oil Tank. In Proceedings of the ASME/BATH Symposium on Fluid Power & Motion Control, Bath, UK, 10–12 September 2014; pp. 1–6, doi:10.1115/FPMC2014-7834.
10. Schmidt, L.; Roemer, D.B.; Pedersen, H.C.; Andersen, T.O. Speed-Variable Switched Differential Pump System for Direct Operation of Hydraulic Cylinders. In Proceedings of the ASME/BATH Symposium on Fluid Power & Motion Control, Chicago, IL, USA, 12–14 October 2015.
11. Schmidt, L.; Groenkjaer, M.; Pedersen, H.C.; Andersen, T.O. Position Control of an Over-Actuated Direct Hydraulic Cylinder Drive. *Control Eng. Pract.* **2017**, *64*, 1–14, doi:10.1016/j.conengprac.2017.04.003.
12. Brahmer, B. Hybrid Drive using Servo Pump in Closed Loop. In Proceedings of the 8th International Fluid Power Conference, Dresden, Germany, 26–28 March 2012; pp. 93–102.
13. Cleasby, K.; Plummer, A.; Company, T. A novel high efficiency electrohydrostatic flight simulator motion system. In Proceedings of the ASME/BATH Symposium on Fluid Power & Motion Control, Bath, UK, 10–12 September 2008; pp. 437–449.
14. Neubert, T. Elektro-hydraulische antriebssysteme mit drehzahlveränderbaren Pumpen. In Proceedings of the Internationales Fluidtechnisches Kolloquium, Aachen, Germany, 17–18 March 1998. (In German)
15. Gøytil, P.; Padovani, D.; Hansen, M.R. On the Energy Efficiency of Dual Prime Mover Pump-Controlled Hydraulic Cylinders. In Proceedings of the ASME/BATH Symposium on Fluid Power & Motion Control, Longboat Key, FL, USA, 7–9 October 2019.
16. Ketelsen, S.; Padovani, D.; Andersen, T.O.; Ebbesen, M.K.; Schmidt, L. Classification and Review of Pump-Controlled Differential Cylinder Drives. *Energies* **2019**, *12*, 1293, doi:10.3390/en12071293.
17. Grønkær, N.; Hansen, K.V.; Johansen, P.; Schmidt, L. Tribotronics in Electro-Hydraulic Actuator Technology: Improving Durability by Control. In Proceedings of the ASME/BATH Symposium on Fluid Power & Motion Control, Virtual, Online, 9–11 September, 2020.
18. Qu, S.; Fassbender, D.; Vacca, A.; Busquets, E.; Formulation, Design and Experimental Verification of an Open Circuit Electro-Hydraulic Actuator. In Proceedings of the 2020 IEEE Global Fluid Power Society PhD Symposium (GFPS), Online, 19–21 October 2020.
19. Qu, S.; Fassbender, D.; Vacca, A.; Busquets, E.; Neumann, U. A Closed Circuit Electro-Hydraulic Actuator with Energy Recuperation Capacity. In Proceedings of the 12th International Fluid Power Conference, Dresden, Germany, 12–14 October 2020; pp. 89–98.
20. Zagar, P.; Kogler, H.; Scheidl, R.; Winkler, B. Hydraulic switching control supplementing speed variable hydraulic drives. *Actuators* **2020**, *9*, 1–13, doi:10.3390/act9040129.
21. Schmidt, L.; Ketelsen, S.; Brask, M.H.; Mortensen, K.A. A Class of Energy Efficient Self-Contained Electro-Hydraulic Drives with Self-Locking Capability. *Energies* **2019**, *12*, 1866, doi:10.3390/en12101866.

22. Schmidt, L.; Ketelsen, S.; Padovani, D.; Mortensen, K.A. Improving the Efficiency and Dynamic Properties of a Flow Control Unit in a Self-Locking Compact Electro-Hydraulic Cylinder Drive. In Proceedings of the ASME/BATH Symposium on Fluid Power & Motion Control, Longboat Key, FL, USA, 7–9 October 2019.
23. Padovani, D.; Ketelsen, S.; Hagen, D.; Schmidt, L. A Self-Contained Electro-Hydraulic Cylinder with Passive Load-Holding Capability. *Energies* **2019**, *12*, 292, doi:10.3390/en12020292.
24. Ketelsen, S.; Andersen, T.O.; Ebbesen, M.K.; Schmidt, L. A Self-Contained Cylinder Drive with Indirectly Controlled Hydraulic Lock. Modelling, Identification & Control **2020**, *41*, 185–205, doi:10.4173/mic.2020.3.4.
25. Hagen, D.; Padovani, D.; Choux, M. A Comparison Study of a Novel Self-Contained Electro-Hydraulic Cylinder versus a Conventional Valve-Controlled Actuator—Part 1 : Motion Control. In *Actuators*; Multidisciplinary Digital Publishing Institute: Basel, Switzerland, 2019.
26. Ketelsen, S.; Kolks, G.; Andersen, T.O.; Schmidt, L.; Weber, J. Bootstrap Reservoir Concepts for Electro-hydraulic Compact Cylinder Drives. In Proceedings of the 12th International Fluid Power Conference, Dresden, Germany, 12–14 October 2020.
27. Ketelsen, S.; Padovani, D.; Ebbesen, M.K.; Andersen, T.O.; Schmidt, L. A Gasless Reservoir Solution for Electro-Hydraulic Compact Drives with Two Prime Movers. In Proceedings of the ASME/BATH Symposium on Fluid Power & Motion Control, Online, 9–11 September 2020.
28. Bucher Hydraulic. *AX Series Piston Pumps and Motors*; Bucher Hydraulic: Klettgau, Germany, 2019.
29. Hagen, D.; Padovani, D.; Choux, M. A Comparison Study of a Novel Self-Contained Electro-Hydraulic Cylinder versus a Conventional Valve-Controlled Actuator—Part 2 : Energy Efficiency. In *Actuators*; Multidisciplinary Digital Publishing Institute: Basel, Switzerland, 2019.
30. Qu, S.; Fassbender, D.; Vacca, A.; Busquets, E. A High-Efficient Solution for Electro-Hydraulic Actuators with Energy Regeneration Capability. *Energy* **2021**, *216*, 119291, doi:10.1016/j.energy.2020.119291.
31. Minav, T.; Bonato, C.; Sainio, P.; Pietola, M. Position control of direct driven hydraulic drive. In Proceedings of the 9th International Fluid Power Conference, Aachen, Germany, 24–26 March 2014, doi:10.1115/FPNI2014-7823.
32. Love, L.; Lanke, E.; Alles, P. *Estimating the Impact (Energy, Emissions and Economics) of the US Fluid Power Industry*; Technical Report December; Oak Ridge National Laboratory (ORNL): Oak Ridge, TN, USA, 2012; doi:10.2172/1061537.
33. Ketelsen, S.; Schmidt, L.; Donkov, V.; Andersen, T. Energy saving potential in knuckle boom cranes using a novel pump controlled cylinder drive. *Model. Identif. Control* **2018**, *39*, doi:10.4173/mic.2018.2.3.
34. Ketelsen, S.; Andersen, T.O.; Ebbesen, M.K.; Schmidt, L. Mass Estimation of Self-Contained Linear Electro-Hydraulic Actuators and Evaluation of the Influence on Payload Capacity of a Knuckle Boom Crane. In Proceedings of the ASME/BATH Symposium on Fluid Power & Motion Control, Longboat Key, FL, USA, 7–9 October 2019.
35. Padovani, D.; Ketelsen, S.; Schmidt, L. Downsizing the Electric Motors of Energy Efficient Self-Contained Electro-hydraulic Systems by Hybrid Technologies. In Proceedings of the ASME/BATH Symposium on Fluid Power & Motion Control, Online, 9–11 September 2020.
36. Minav, T.; Sainio, P.; Pietola, M. Efficiency of Direct Driven Hydraulic Setup in Arctic Conditions. In Proceedings of the Fourteenth Scandinavian International Conference on Fluid Power, Tampere, Finland, 20–22 May 2015.
37. Minav, T.; Papini, L.; Pietola, M. A Thermal Analysis of Direct Driven Hydraulics. In Proceedings of the 10th International Fluid Power Conference, Dresden, Germany, 8–10 March 2016; pp. 235–247.
38. Minav, T.; Pietola, M. A study on thermal behavior of pump-controlled actuator. In Proceedings of the 15th Scandinavian International Conference on Fluid Power, Linköping, Sweden, 7–9 June 2017, doi:10.1115/1.3253248.
39. Grønkær, N.; Nielsen, L.N.; Nielsen, F.Ø.; Ketelsen, S.; Schmidt, L. Multi-Objective Control of a Self-Contained Compact Electro-Hydraulic Cylinder Drive. In Proceedings of the 12th International Fluid Power Conference, Dresden, Germany, 12–14 March 2020.
40. Michel, S.; Schulze, T.; Weber, J. Energy-efficiency and thermo energetic behaviour of electrohydraulic compact drives. In Proceedings of the 9th International Fluid Power Conference, Aachen, Germany, 24–26 March 2014.
41. Michel, S.; Weber, J. Prediction of the thermo-energetic behaviour of an electrohydraulic compact drive. In Proceedings of the 10th International Fluid Power Conference, Dresden, Germany, 8–10 March 2016; pp. 219–234.
42. Sidders, J.A.; Tilley, D.G.; Chappie, P.J. Thermal-Hydraulic Performance Prediction in Fluid Power Systems. *Proc. Inst. Mech. Eng. Part I J. Syst. Control Eng.* **1996**, *210*, 231–242, doi:10.1243/PIME_PROC_1996_210_462_02.
43. Munson, B.R.; Young, D.F.; Okiishi, T.H.; Huebsch, W.W. In *Fundamentals of Fluid Mechanics*, 6th ed.; John Wiley & Sons: Hoboken, NJ, USA, 2010.
44. Cengel, Y.A.; Boles, M.A. *Thermodynamics : An Engineering Approach*, 5th ed.; McGraw-Hill: New York, NY, USA, 2006.
45. Knežević, D. Analysis of Changes of Bulk Modulus of Mineral Oil. In Proceedings of the 12th International Conference on Tribology, Kragujevac, Serbia, 11–13 May 2011.
46. Cengel, Y.A.; Cimbala, J.M.; Turner, R.H. *Fundamentals of Thermal-Fluid Sciences*, 4th ed.; McGraw-Hill: New York, NY, USA, 2012; p. 1083.
47. Smith, J.; Van Ness, H.; Abbott, M. *Introduction to Chemical Engineering Thermodynamics*, 6th ed.; McGraw-Hill: New York, NY, USA, 2001.

48. Brun Hansen, H.; Windfeld Rasmussen, P. Modeling Hydraulic Accumulators for use in Wind Turbines. In Proceedings of the 13th Scandinavian International Conference on Fluid Power, Linköping, Sweden, 3–5 June 2013; Volume 92, pp. 327–334, doi:10.3384/ecp1392a32.
49. Liniger, J. Design of Reliable Fluid Power Pitch Systems for Wind Turbines. Ph.D. Thesis, Aalborg University, Aalborg, Denmark, 2018.
50. Liniger, J.; Sepehri, N.; Soltani, M.; Pedersen, H.C. Signal-based gas leakage detection for fluid power accumulators in wind turbines. *Energies* **2017**, *10*, doi:10.3390/en10030331.
51. Busquets, E.; Ivantysynova, M. Temperature prediction of displacement controlled multi-actuator machines. *Int. J. Fluid Power* **2013**, *14*, 25–36, doi:10.1080/14399776.2013.10781066.
52. Rituraj, R.; Vacca, A.; Morselli, M.A. Thermal modelling of external gear machines and experimental validation. *Energies* **2020**, *13*, 1–24, doi:10.3390/en13112920.
53. Pfeffer, A.; Glück, T.; Kemmetmüller, W.; Kugi, A. Mathematical modelling of a hydraulic accumulator for hydraulic hybrid drives. *Math. Comput. Model. Dyn. Syst.* **2016**, *22*, 397–411, doi:10.1080/13873954.2016.1174716.
54. Moran, M.; Shapiro, H. *Fundamentals of Engineering Thermodynamics*, 5th ed.; John Wiley & Sons: Hoboken, NJ, USA, 2006.
55. Oppermann, M. A new approach for failure prediction in mobile hydraulic systems. Ph.D. Thesis, Hamburg University of Technology, Hamburg, Germany, 2007.
56. Chenggong, L.; Zongxia, J. Calculation Method for Thermal-Hydraulic System Simulation. *J. Heat Transf.* **2008**, *130*, doi:10.1115/1.2928006.
57. Knežević, D.; Savić, V. Mathematical Modelling of Changing of Dynamic Viscosity, as a Function of Temperature and Pressure of Mineral Oils for Hydraulic Systems. *Mech. Eng.* **2006**, *4*, 27–34.
58. Michel, S.; Weber, J. Electrohydraulic Compact-drives for Low Power Applications considering Energy-efficiency and High Inertial Loads. In Proceedings of the 7th FPNI PhD Symposium on Fluid Power, Reggio Emilia, Italy, 27–30 June 2012; pp. 1–18.
59. Verein Deutscher Ingenieure. *VDI Heat Atlas*, 2nd ed.; VDI-Verlag GmbH: Dusseldorf, Germany, 2010, doi:10.1007/978-3-540-77877-6.
60. Verein Deutscher Ingenieure. *VDI-Wärmeatlas*, 11th ed.; Springer: Berlin/Heidelberg, Germany, 2013.
61. Jungnickel, G. *Simulation des Thermischen Verhaltens von Werkzeugmaschinen*; TU-Dresden: Dresden, Germany, 2010.
62. Ruderman, M. Full- and Reduced-order Model of Hydraulic Cylinder for Motion Control. In Proceedings Proceedings of the IECON 2017 - 43rd Annual Conference of the IEEE Industrial Electronics Society, 29 October–1 November 2017.
63. Ottestad, M; Hansen, N, Hansen, M.R. Reducing the Static Friction in Hydraulic Cylinders by Maintaining Relative Velocity Between Piston and Cylinder . In Proceedings of the 12th International Conference on Control, Automation and Systems, Jeju Island, Korea, 17–21 October 2017.
64. Li, P.; Barkei, J.H. Hydraulic Effort and the Efficiencies of Pump and Motor with Compressible Fluid. In Proceedings of the ASME/BATH Symposium on Fluid Power & Motion Control, Online, 9–11 September, 2020.